ACS APPLIED NANO MATERIALS

Determining the Elastic Modulus of Microgel Particles by Nanoindentation

Nadine Raßmann,○ Steffen Trippmacher,○ Agnes Specht, Katinka Theis, Tamino Rößler, Sebastian Wohlrab, Richard Kellnberger, Sahar Salehi, Hendrik Bargel, Nicolas Helfricht, Krystyna Albrecht, Thomas Scheibel, Jürgen Groll, Stephan Gekle, and Georg Papastavrou*

Cite This: https://doi.org/10.1021/acsanm.4c06964 Read Online

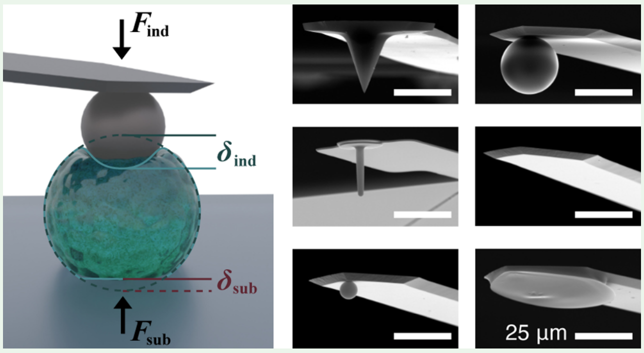

ABSTRACT: The mechanical properties of materials and cells are key factors for many processes in biofabrication. Nanoindentation using atomic force microscopy represents an important technique to quantify the Young's elastic modulus in a locally resolved manner or for single microgel particles and cells, respectively. Here, we address the question of the best-suited indenter geometry and continuum model for contact mechanics to describe the nanoindentation of microgels. Two different microgel model systems have been synthesized using microfluidics with a very narrow size distribution of the particles: poly(acrylamide) and ene-functionalized polyoxazoline/thiol-functionalized hyaluronic acid. The respective microgel particles have been characterized by up to six different types of indenter geometries, including spherical, parallel plate, and cone. Moreover, the influence of experimental parameters, such as indentation depth and velocity, on the resulting Young's modulus has been studied. Compared to the Hertz model, the simplified double contact model (SDC model) provided a better description of the indentation process and a narrower distribution of Young's moduli with respect to the different indenter geometries. By numerical simulation of the indentation process, we demonstrated that the remaining variation of the Young's moduli is attributed to adhesion. The adhesive force between a particle and the substrate led to a prestress, which is similar to that of particle deformation by the substrate as accounted for by the SDC model. This effect varied in strength with the indenter geometries and can contribute significantly to the experimentally observed variation of Young's moduli for different indenter geometries. Importantly, these results can also be extended to the indentation of single living cells.

KEYWORDS: *AFM, hydrogel, soft matter, elasticity, nanoindentation, adhesion, cells*

■ INTRODUCTION

The mechanical properties of cells, sometimes also referred to as mechanical phenotype, provide direct access to the physiological state of a cell.[1,2] For example, the elastic modulus of the underlying substrate or surrounding matrix plays an important role in the development and regeneration of stem cells.[3,4] Some diseases, such as cancer, sickle cell anemia, and malaria, to name only a few, result in significant changes in cell mechanics. Hence, cell mechanics and pathogenesis of human disease are often related, and the former can be used for diagnostic purposes.[5−8] Thus, the mechanical properties of cells have been studied extensively.[5,7,9−13] However, cell elasticity can vary over time and locally on the cell, as e.g., the cytoskeleton and the cell nucleus show deviating elastic moduli. Microgel particles are a widely used model system that allows mimicking cells in biomaterials research being more constant and homogeneous in terms of its elastic properties.[14−17] Therefore, the microgel particles allow to verify characterization methods for applications with cells.[18] The size and elasticity of microgels can be easily tuned to match the properties of cells during synthesis, e.g., by varying the cross-linking density.[17−20] Micromechanical properties are key characteristics of microgels, and the Young's modulus is a typical measure of choice to characterize the elasticity of soft matter such as cells and microgels.[17,21] Nanoindentation based on atomic force microscopy (AFM),[1,15,16,22,23] besides deformation in a flow channel,[2,24−26] and micropipette aspiration,[12,27] are the most widely used techniques to study Young's moduli of cells and microgels. While microfluidic-based methods deform the entire particle,[2,24] capillary

Received: December 10, 2024
Revised: February 10, 2025
Accepted: February 11, 2025

aspiration[12,27] and AFM nanoindentation[18,22,23] cause more local deformations.[1,16,20] In a typical AFM nanoindentation experiment, a cantilever equipped with a sharp tip or spherical colloidal particle is indented into the sample.[18,22,28−30] The resulting force vs indentation data can be fitted to various mechanical contact models that allow extracting elastic properties.[21] For a long time, Hertzian contact mechanics represented the quasi-standard for data analysis.[5,10,31] The Hertz model assumes that the cell or microgel can be approximated as an infinite elastic half-sphere. Moreover, no adhesion between the indenter and sample is supposed to be acting.[21,32] However, small samples, such as cells and microgel particles, have to be placed on a planar substrate in order to perform nanoindentation experiments on them. It is known that, the underlying substrate can lead to a significant overestimation of the Young's modulus for thin films,[33,34] especially in the case when the indentation depth is larger than 10% of the film thickness.[35,36] To account for this effect, models to compensate for the contribution of the substrate have been introduced.[36] Recently, it has been demonstrated that also for small spherical soft samples, like microgels or cells, the presence of a hard substrate can lead to significant deviations from the classical Hertz model.[11,12] As a first approximation, thin-film models have been applied to describe deep indentations on small microgel particles.[22,37] However, there is some evidence that soft spherical objects are also deformed at their interface with the substrate while being indented from the top.[11,12,18,38] This effect cannot be described adequately by thin-film models. Approximating cells and microgels as elastic hemispheres and neglecting the bottom deformation can significantly underestimate the Young's modulus, depending on the microgel and indenter characteristics.[38]

First, Dokukin et al. introduced a double contact model to describe loosely attached cells on nondeformable surfaces, thereby accounting for the additional cell deformation by the substrate during the indentation measurement.[11] This approach has been refined by Glaubitz et al., presenting a more general form for spherical samples, including the effects of predeformation, and discussing the theory of a variety of size ratios between particle, indenter, and substrate radii.[38] Later, Daza et al. adapted the model for conical indenters and reported a significant decrease in the deviation of Young's moduli as determined by AFM-based indentation experiments compared to micropipette aspiration.[12] While these "double-contact models" were introduced nearly a decade ago, they have been applied only sparsely so far.[11,12,18,38−40] One reason could be that a systematic comparison for highly defined systems, such as microgel particles, has not been reported yet, and research concentrated primarily on more complex biological systems, such as cells. Such a systematic comparison needs to include different indenter geometries as those will affect the Young's moduli derived by the double-contact model differently.[38]

The best-suited indenter geometry for soft samples, such as cells and microgels, has been discussed extensively in the past.[30,41−44] While micrometer-sized colloidal probes provide a well-defined geometry, they cannot account for laterally resolved variations in elasticity commonly observed in cells. On the other hand, nanometer-sized sharp tips might fall on a length scale where continuum models cannot always be inherently assumed for hydrogels. In recent years, purposely constructed AFM cantilevers hybridizing both aspects are increasingly used.[43,45] Several studies observed significant deviations between elastic moduli when comparing indentation using sharp tips and spherical indenters.[10,18,28−31,40,42−44] This finding requires attention as the Young's modulus of microgels, or cells, is an intrinsic material property and should, therefore, be independent of the indenter geometry provided that a suitable continuum model has been applied to describe the mechanical response. Therefore, elastic continuum models to describe AFM-based indentation experiments must also account for the indenter geometry.

Here, we studied the validity of the simplified double contact model (SDC model) and the effect of different indenter geometries for two highly defined microgels as model systems: microgels based on polyacrylamide (PAAm),[18] as well as ene-functionalized polyoxazoline (POx) together with a thiol-functionalized hyaluronic acid (POx-HASH).[46,47] Both microgel systems were synthesized using microfluidics, resulting in a narrow distribution of diameters of ∼25−30 μm and Young's moduli in a cell-relevant range (<10 kPa). By utilizing two different hydrogel systems originating from very different synthetic routes, we can exclude that the described mechanical properties are hydrogel specific. PAAm is a fully synthetic polymer that has been used in the past as a model for nanoindentation experiments and thus allows for a classification of the here-performed experiments.[18] In contrast, POx-HASH is a hybrid of ene-functionalized polyoxazoline and thiol-functionalized hyaluronic acid. It has been only recently introduced, primarily for biofabrication purposes.[46,47] This hybrid polymer system combines the stiffer POx with the more elastic HASH to obtain elastic moduli in a cell-similar range. We compared up to six different indenter geometries in the AFM-based nanoindentation experiments. Our experimental results clearly favor the double-contact model. The remaining discrepancies between the different indenter geometries could be explained based on theoretical simulations considering the prestress due to the adhesive contact between the microgel particle and the substrate. Besides the indenter geometry, we demonstrate the importance of choosing adequate measurement parameters, such as the proper alignment of the indenter to the microgel apex, the indentation velocity, and the loading force.

■ EXPERIMENTAL METHODS

Materials. All aqueous solutions were prepared with Milli-Q water (IQ 7000, resistivity: 18 MΩ cm, Merck KGaA, Darmstadt, Germany). Ammonia 25% (VWR International S. A. S, Rosny-sous-Bois, France), Krytox 157 FSH (H. Costenoble GmbH & Co. KG, Eschborn, Germany), methanol (Fisher Scientific, Loughborough, UK), ethanol (p.A. VWR Chemicals, Darmstadt, Germany), HFE 7100 (IOLITEC GmbH, Germany), Sylgard 184 elastomer kit (Mavom GmbH, Steinfurt, Germany), 2-propanol (VWR International S. A. S, France), acrylamide (AAm, ≥99%, Sigma-Aldrich, St. Louis, MO, USA), *N*,*N*′-methylenbis(acrylamide) (BIS, 99%, Sigma-Aldrich, USA), *N*-(3-aminopropyl)methacrylamide hydrochloride (APMA, 98%, Sigma-Aldrich, USA), ammonium persulfate (APS, 98%, Sigma-Aldrich, USA), *N*,*N*,*N*′,*N*′-tetramethylethylenediamine (TEMED, ≥99%, Sigma-Aldrich, USA), 1H,1H,2H,2H-perfluoro-1-octanol (97%, Sigma-Aldrich, USA), phosphate buffered saline (1× PBS, pH 7.4, Sigma-Aldrich, USA), fluorescein 5-isothiocyanate (5-FITC, ≥90%, Cayman Chemical Company, Ann Arbor, MI, USA), SU-8 2015, SU-8 2050 photoresist and SU-8 developer (micro resist technology GmbH, Berlin, Germany), Hellmanex III (Hellma GmbH & Co. KG, Müllheim, Germany), isopropyl alcohol (p.a. VWR Chemicals, Darmstadt, Germany), hydrogen peroxide (30 w/v %, Fisher Scientific, Schwerte, Germany), lithium-phenyl-2,4,6-trimethylbenzoylphosphinate (LAP, TCI Chemicals, Eschborn, Germany), Span 80 (Sigma-Aldrich, Darmstadt, Germany), 3-aminopropyldimethylethoxysilane (APDMES, 97%, abcr, Karlsruhe, Germany) and mineral oil (Sigma-Aldrich, Darmstadt, Germany) were used as received.

Surfactant Synthesis. The surfactant was synthesized with minor modifications as described by Girardo et al.[18] Briefly, 10 g Krytox 157 FSH were dissolved in 60 mL methanol and 30 mL HFE 7100. Subsequently, 25 mL 0.1 M ammonia was added slowly over a dropping funnel. After overnight reaction, solvents were removed at the rotary evaporator, and the obtained oil was further dried under reduced pressure and at 80 °C overnight. The viscous oil was stored at room temperature in an amber glass vial.

Microfluidic-Assisted Synthesis of PAAm-Particles. The synthesis of PAAm-particles follows a modified procedure based on Girardo et al.[18] First, the monomer solution of AAm and BIS with a total monomer content of 18.6% (w/v) and a BIS/AAm-ratio of 3.25% (w/w) was prepared. The solution was purged with argon for 30 min. Meanwhile, pure water was also purged with argon for 30 min. Afterward, APS was dissolved in purged water (16 g L^{-1}).

For FITC-labeling of PAAm, a modified procedure of Hu et al. has been followed.[48] In difference to the preparation of bare PAAm particles, 5 mol % of AAm were replaced by APMA. The oil phase consisted of 1.5% (w/w) surfactant (synthesized) and 0.4% (v/v) TEMED in HFE7500. No purging with argon has been done.

A microfluidic device was used for particle synthesis. Details on the device fabrication are available in the Supporting Information. The device was connected to two reservoirs via PEEK-tubing (1/32" OD × 0.010" ID, BGB Analytik Vertrieb GmbH, Lörrach, Germany). Two 2 mL vials acted as reservoirs. One vial was filled with 1 mL of oil phase; the other vial was filled with 300 μL monomer solution and 300 μL APS solution. The two aqueous solutions were mixed gently to minimize the dissolution of oxygen. The reservoirs were set under pressure by Flow EZ pressure controllers (Fluigent, Le Kremlin-Bicêtre, France) with additional Flow Unit S flow sensors (Fluigent, Le Kremlin-Bicêtre, France) enabling droplet formation under flow control. The flow rates during droplet formation were 300 μL h^{-1} for the aqueous phase and 750 μL h^{-1} for the oil phase. The droplets were collected in another vial containing 500 μL oil phase. Twenty minutes after mixing the aqueous phase, the procedure was stopped. The resulting emulsion was shaken overnight at 20 °C (800 rpm). Afterward, the emulsion rested for the clear oil phase to settle. The clear oil was removed, and 500 μL emulsion breaker (20% (v/v) PFO in HFE7500) were added. The mixture was vortexed for 10 s and then centrifuged at 5000*g* for 1 min. The oil phase was removed, and 500 μL *n*-hexane were added. The mixture was vortexed for 10 s and then centrifuged (5000*g*, 1 min). *n*-Hexane was removed, and 100 μL of phosphate-buffered saline (PBS) were added. In the case of the particles modified by APMA, 300 μL of PBS were added. The particle suspension was stored at 4 °C. The stock suspension was diluted by adding PBS.

FITC-Labeling of PAAm Microgel Particles. The particles modified with APMA (150 μL stock suspension) were added to 2 mL of a 0.1 mg mL^{-1} FITC solution in PBS. The suspension was shaken overnight at 20 °C (800 rpm). Then, the particles were centrifuged off (8000*g*, 2 min). The residue was resuspended in 1.5 mL PBS. The process of centrifugation and resuspension was repeated six times. After the final centrifugation, the particles were resuspended in 500 μL PBS and stored at 4 °C.

Microfluidic-Assisted Synthesis of POx-HASH Microgel Particles. For the synthesis, an ene-functionalized polyoxazoline (POx) and a HASH were used, which were synthesized as described previously.[46,47] The pregel solution was obtained by dissolving POx and HASH, each with a concentration of 3.75% (w/v) in PBS buffer, pH 7.4, to obtain a total polymer content of 7.5% (w/v). Lithium-phenyl-2,4,6-trimethylbenzoylphosphinate was added to the aqueous solution in a concentration of 1% (w/v) as a photoinitiator for photo-cross-linking. Before use, the polymer solution was filtered through a 17 mm syringe filter (cellulose membrane with a pore diameter of 0.2 μm). The oil phase consisted of mineral oil and 2.5% (w/v) Span 80. The mixed precursor solutions were transferred to glass syringes (SYR 1 mL 1001 TLL for the aqueous phase, 2 x SYR 5 mL 1005 TLL for the oil phase, Hamilton) that were installed into displacement-based syringe pumps (neMESYS, Cetoni GmbH, Korbussen, Germany). Using Luer–Lock connections, the syringes were connected to PE tubings (I.D. 0.28 mm, O.D. 0.64 mm, Scientific Commodities Inc., Lake Havasu City, USA) via precision tips (TIP 30GA 0.006×.25, Nordson EFD, West Lake, USA). The PE tubes were connected to the inlet chambers of the microfluidic device (oil phases to the two outer inlets, polymer phase to the middle inlet. Details on the device fabrication are stated in the Supporting Information). The flow was adjusted using the QmixElements software (Cetoni GmbH, Korbussen, Germany) to control the syringe pumps. Flow rates were 460 μL h^{-1} (each, 920 μL h^{-1} in total) for the oil phase and 48 μL h^{-1} for the aqueous phase. A high-framerate video camera (Phantom v1610, Vision Research Inc., Charlottetown, Canada) attached to a light microscope (Axio Vert.A1 FL, Zeiss, Oberkochen, Germany) was used to observe droplet production. After droplet formation on the chip, the droplets were exposed to a 405 nm power LED (Silver-LED-405, Fiber Coupled UV, Prizmatix, Holon, Israel) for photo-cross-linking via a thiol-ene click reaction in flow in a PE tubing connected to the outlet chamber of the microfluidic device for 5 s. The resulting microgel suspension in oil was collected in a 10 mL glass vial. The produced microgel beads in oil were washed two times via centrifugation (11,500*g*, 2.5 min) in *n*-hexane and three times via centrifugation (11,500*g*, 2.5 min) in 1× PBS. The final aqueous bead solution was stored at 4 °C.

Surface Functionalization and Cleaning. PAAm microgel particles were immobilized on freshly cleaned glass discs, while POx-HASH microgel particles were immobilized on APDMES-modified glass discs, respectively. Briefly, circular glass discs (diameter: 35 mm, Irlbacher Blickpunt Glas, Schönsee, Germany) were cleaned by a modified three-step RCA cleaning procedure. The glass discs were sonicated in 2% (v/v) Hellmanex III (Hellma GmbH & Co. KG, Müllheim, Germany) in Milli-Q grade water at 40 °C for 20 min and were rinsed extensively with Milli-Q water. Next, the glass discs were sonicated in a 3:1 (v/v) mixture of isopropyl alcohol and Milli-Q water. Afterward, the glass was thoroughly washed with Milli-Q water. In a third step, the glass discs were exposed to a 5:1:1 (v/v/v) mixture of Milli-Q water, ammonia, and hydrogen peroxide at 80 °C for 20 min. Finally, the glass discs were rinsed extensively with Milli-Q water and dried under a nitrogen stream. Directly before surface modification, the discs were rinsed again with Milli-Q water, ethanol (EtOH), and Milli-Q water and dried under a nitrogen stream. The surface was activated by exposure to air plasma (Zepto, Diener Electronics, Ebhausen, Germany) for 20 min. If needed, the glass discs were coated with APDMES via vapor deposition at reduced pressure in a desiccator overnight. APDMES-modified slides were rinsed with Milli-Q water, EtOH, and Milli-Q water and dried under a stream of nitrogen. The success of the surface functionalization was verified by measuring the static water contact angle (>60°).

AFM-Cantilever Calibration and Preparation of Colloidal Probes. Six different types of indenter geometries were realized based on three kinds of AFM cantilevers: tipless (HQ:CSC37B/tipless/Cr–Au, MikroMasch, Sofia, Bulgaria), sharp tip (CSCS12E, MikroMasch, Sofia, Bulgaria), and rounded-tip (SAA-SPH-1UM, Bruker Nano Surfaces, Wissembourg, France), with nominal resonance frequencies of 20, 12, and 40 kHz, and nominal spring constants of 0.3, 0.04 and 0.25 N m^{-1}, respectively. Please notice that the CSCS12E cantilevers are not produced anymore and were from an old stock in our laboratory. Sharp-tip and rounded-tip cantilevers were used as conical or spherical indenters without further modification. Spherical indenters with larger diameters, so-called colloidal probes, were fabricated by attaching two types of silica microspheres, small (d_{nom} = 6.80 μm, Bangs Laboratories, Fishers, USA) and large (d_{nom} = 24.77 μm, microParticles GmbH, Berlin, Germany), to the free end of the tipless cantilevers (HQ:CSC37B/tipless/Cr–Au, MikroMasch, Sofia, Bulgaria). First, a small droplet of UV curable glue (NOA 63, Norland Adhesives, Norland Products, Jamesburg, USA) was placed on the free end using etched tungsten wires employing a

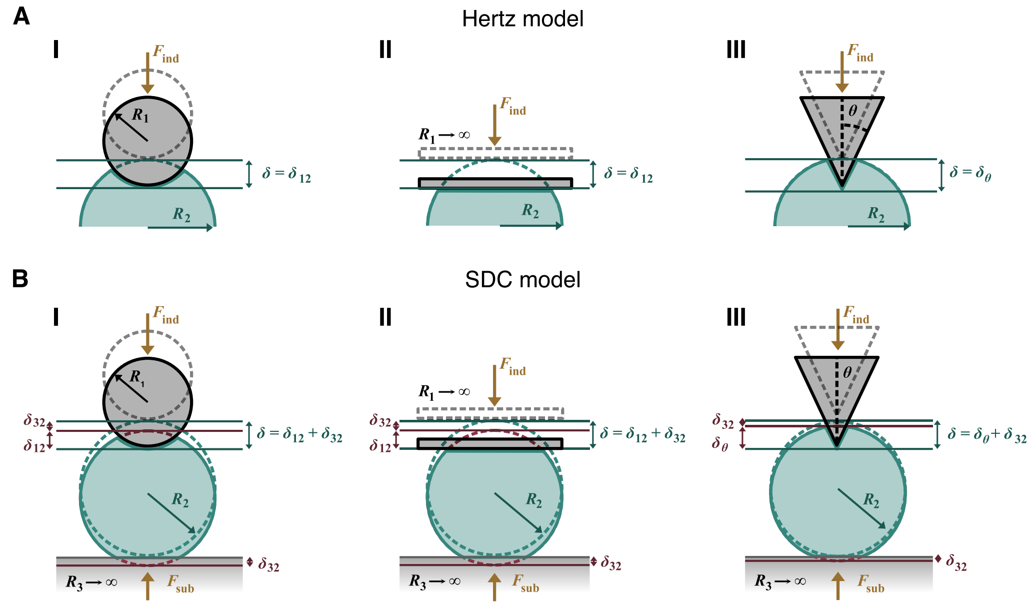

Figure 1. Schematic of the contact models describing the nanoindentation of microgel particles using three different indenter geometries: I: sphere, II: plane, and III: cone. (A) The simple Hertz model describes the indentation of the indenter into the soft hydrogel particle. The deformation generated by the force applied to the indenter is limited to the indenter−sample contact. (B) The SDC model accounts for the deformation at the tip−sample interface and the force exerted on the microgel by the substrate when the tip indents the sample.

micromanipulator (DC-3 KS, Märzhäuser, Ebhausen, Germany) under the control of a fixed-stage microscope (Examiner D.1, Zeiss, Oberkochen, Germany). Subsequently, the respective microsphere was manipulated onto the glue droplet, and the glue was cured by exposure to UV light. Tipless cantilevers without modification were used as planar indenters. Furthermore, wedged cantilevers, which compensate for the 10° tilt angle of the MFP-3D cantilever holder, were fabricated using a modified procedure based on Stewart et al.[49] (details are available in the Supporting Information).

The spring constants of all cantilevers (HQ:CSC37B/tipless/Cr−Au, CSCS12E, MikroMasch, Sofia, Bulgaria) besides the precalibrated rounded-tip probes (SAA-SPH-1UM, Bruker, Nano Surfaces, Wissembourg, France) were calibrated according to the thermal noise method[50] in air before conducting the first measurements. Colloidal probes were calibrated in all cases before attaching the particle to the cantilever. The determined spring constant seems not to depend on order, i.e., attachment of particle or spring constant calibration, for the thermal noise method.[51] Spring constants ranged between 0.21−0.40 N m^{-1} and 0.02−0.08 N m^{-1} for the tipless and sharp tip cantilevers, respectively.

Cantilevers were cleaned by repeatedly dipping into several solvents (Milli-Q water, ethanol, isopropanol, ethanol, Milli-Q water) and exposure to air plasma (Zepto, Diener electronic, Ebhausen, Germany) for 120 s prior to usage. Subsequently, we functionalized the cantilevers by immersion into a 1 g L^{-1} solution of poly(L-lysine)-*graft*-poly(ethylene glycol) (PLL-*g*-PEG) (SuSoS Surface Technologies, Dübendorf, Switzerland) in Milli-Q water for >30 min to minimize adhesion to the microgel beads. Excess PLL-*g*-PEG was rinsed off by dipping into Milli-Q water.

Nanoindentation Experiments. AFM-based nanoindentation measurements were conducted on a MFP-3D AFM (Asylum Research, Oxford Instruments, Santa Barbara, USA) mounted on top of an inverted optical microscope (Axio Observer Z.1, Zeiss, Oberkochen, Germany) equipped with a 20× objective and a brightfield cube. A commercial fluid cell (Asylum Research, Oxford Instruments, Santa Barbara, USA) with an exchangeable glass disc bottom allowed for optical control during all experiments. Glass discs were modified with APDMES by vapor deposition to immobilize POx-HASH microgels. For PAAm, glass discs were used after plasma activation (air plasma, 20 min) without further modification. The glass discs were mounted to the fluid cell, and 30 μL of the microgel suspension was placed into the cell. A few droplets of phosphate-buffered saline (PBS) were added to ensure complete wetting of the glass disc. The microgel beads were left to sediment for 15 min before exchanging the buffer in the cell three times and filling the fluid cell to its total volume of ∼2.5 mL PBS.

Proper center−center alignment was ensured by acquiring an array of force−distance curves on an 8 × 8 grid of 4 μm × 4 μm. A height map was calculated in the AR software (AR v.16.33.234, Asylum Research, Oxford Instruments, Santa Barbara, USA) by evaluating the z-sensor position when the preset trigger point was reached. The internal nudger function of the AFM was used to position the cantilever over the apex of the microgel bead. In contrast to all other indenter geometries, the coarse optical alignment of the tipless and wedged cantilevers was sufficient due to the absence of any indenter curvature.

Indentation measurements at the apex of a microgel bead were conducted by ramping the respective cantilever at a ramping velocity of 0.5 μm s^{-1} to the microgel bead until a predefined deflection was reached. The trigger deflection was chosen so that the indentation depth accounted for 5% of the microgel radius. Typical loading forces ranged between ∼1−15 nN, dependent on the indenter geometry. For some experiment series, either the indentation depth (∼1−10% equivalent to ∼150 nm−1.5 μm) or the ramping velocity (100 nm s^{-1}−15 μm s^{-1}) was varied to study their influence on the determined Young's moduli systematically. The other parameter remained constant at the standard conditions of 5% indentation depth or 0.5 μm s^{-1}, respectively. For an in-depth study of the centering, 16 × 16 force vs distance curves were acquired on an 8 μm × 8 μm sized grid across the center of the microgel bead. The indentation depth was kept at the typical value of 5%, while the ramping velocity of 2 μm s^{-1} was chosen to minimize instrument drift during the force curve acquisition.

Before acquiring a set of force curves for a specific indenter/particle combination, we performed a number of force curves to determine an adequate setpoint (slightly higher than required). However, the final indentation depth was set during the data evaluation as the upper limit of the elasticity fit (maximum indentation depth). This approach was feasible as we did not observe any changes neither in the curves nor in the evaluated Young's moduli during multiple subsequent indentation cycles for both microgels. It has been verified that the data was consistent regardless whether starting from low or high indentation depths during the load depth-dependent studies.

The inverse optical lever sensitivity (InvOLS) was calibrated for every microgel particle and data set by ramping the cantilever against the substrate next to the microgel on the bare glass surface and evaluating the constant compliance region of the resulting force vs distance curve. Due to the nondeformability of the hard glass disc, a linear deflection response with z-piezo movement is achieved.

AFM Data Analysis. AFM raw data was converted to force vs distance curves by home-written procedures in IGOR Pro (v.8.04, Wavemetrics, Portland, OR, US), which were verified to the results obtained by the commercial software provided by the manufacturer of the instrument (AR v.16.33.234, Asylum Research, Oxford Instruments). The contact point was determined by iterative fitting of the contact model. The elastic properties were determined according to the simplified double contact model (eqs 11−14, Figure 1B)[11,12,38] and compared to the results obtained using the Hertz model (eqs 1−10, Figure 1A).[32]

If not stated otherwise, the indentation fit range of the force was chosen to result in an indentation depth of 5% of the particle radius, typically ∼700−750 nm. The Poisson's ratio was fixed at 0.5 for both particle types, which falls in the range commonly used for hydrogels.[18,52] In the case of PAAm, a value close to 0.5 for the Poisson's ratio has been reported also by other techniques.[53]

SEM Images of Cantilevers. Scanning electron microscopy (SEM) images of AFM cantilevers were acquired at a SEM (Quanta FEG 250, FEI, Hilsboro, USA) after sputter-coating with a 1.0 nm thin layer of platinum. The acceleration voltage was set to 30 kV for the cantilever geometries and 15 kV for close-up images of the cone angle. The working distance was set to 10 mm to acquire SEM images using the ET detector.

Total Internal Reflection Fluorescence Microscopy. FITC-labeled PAAm-*co*-PAPMA particles were immobilized on a WillCo-dish glass bottom dish (GWST-3522, WillCo Wells B.V., Amsterdam, Netherlands). The glass bottom dish was cleaned with ethanol and dried in a stream of nitrogen. Subsequently, the dish was placed in a plasma cleaner (Zepto, Diener Electronics, Ebhausen, Germany) for 20 min to activate the glass surface. Afterward, 20 μL of the particle suspension was placed on the activated glass surface. 150 μL of PBS were added to prevent drying. After 5 min, the dish was filled with PBS.

The contact area of the immobilized particles was imaged using a Leica DMi8 Infinity TIRF microscope (Leica, Wetzlar, Germany) equipped with a DFC9000GT-VSC13730 camera, using an oil immersion objective (HC PL APO 100×/1.47 Oil, Leica Microsystems GmbH, Wetzlar, Germany). The refractive index of the immersion oil was 1.518. A 488 nm laser was used to excite the FITC-labeled particles. After automatic TIRF angle calibration, images of the immobilized particles were taken with a penetration depth setting of the evanescent wave of 70 nm. The azimuth was adapted manually for every image to optimize the TIRF illumination.

Simulations. We simulate the elastic deformation of hydrogel particles via a finite element approach. For this we used an in-house code based on previous studies.[25] The radius of the microgel particle was fixed to 14.5 μm and the Young's modulus to 1 kPa. The Poisson's ratio has been set to 0.48 for numerical reasons. For the force calculation via a finite element approach, the particle was split into 108,810 small tetrahedrons of approximately equal size by the Gmsh algorithm.[54] Assuming the tetrahedrons are small enough, the macroscopic stress resulting from the particle's deformation can be modeled as an individual stress tensor $\underline{\sigma}$ (underline denotes a tensor) for each tetrahedron, which is constant across the tetrahedron's volume. This stress can now be calculated from the well-defined deformation of its tetrahedron. For the implementation, we use the Neo-Hookean model strain energy U[25]

$$U = \frac{\mu}{2}(I - 3) + \frac{\kappa}{2}(J - 1)^2 \tag{1}$$

where $I = \mathrm{Tr}(F^{\mathrm{T}}F)$ and $J = \det(F)$ are derived from the gradient deformation tensor F.[55] The moduli μ and κ are related to the elastic modulus E and the Poisson's ratio ν via

$$\mu = \frac{E}{2(1 + \nu)} \tag{2}$$

$$\kappa = \frac{E}{3(1 - 2\nu)} \tag{3}$$

The Poisson's ratio is set to 0.48 for all simulations as higher values make the problem numerically stiff and lead to numerical instability and long simulation times. For an elastic stress tensor $\underline{\sigma}$, the force $\vec{F}$ acting on each surface triangle of the tetrahedron can be written as

$$\vec{F} = A\underline{\sigma}\hat{n} \tag{4}$$

with A being the area of the triangle and $\hat{n}$ being its normal vector, with the hat indicating that it is a normalized vector of length 1. A third of this force is distributed to each vertex in the triangle. Knowing the force of every vertex in the particle, its trajectory can be calculated using damped classical dynamics. The force was recalculated every time-step. For the point movement in our damped classical dynamics algorithm, we used a Velocity−Verlet algorithm[56] with an additional dampening parameter ξ for stability. It should be noted that these dampened dynamics do not intend to model the physical trajectory that the vertices take but do lead to the correct steady state of minimal energy, which is sufficient for modeling our experiments. Indenters were modeled using exponential potentials of appropriate shape. Since such potentials are not infinitely steep, they may lead to the simulations slightly overestimating the deformation. The force from the indenter acting on each vertex in the particle was calculated from the potential and added to the force caused by the elastic deformation.

For adhesive substrates, a Lennard−Jones potential was used to model adhesion instead of the exponential potential at the substrate location.

$$V(r) = 4\epsilon\left[\left(\frac{\sigma}{r}\right)^{12} - \left(\frac{\sigma}{r}\right)^{6}\right] \tag{5}$$

Here, σ is chosen so that the minimum of the potential is $\frac{1}{5}$ of the particle radius from the wall. Adhesion strength is modeled by the size of the prefactor ϵ.

Because adhesion is a surface effect, a numeric surface integral of the force density on the surface triangles of the particle is performed and distributed to the points instead of evaluating the force at each point of the particle as done for the indenter.

From the adhesion strength and the particle parameters, a dimensionless number Λ arises that can be used to quantify the adhesive strength independent of the specific particle parameters. Λ is the control parameter for our simulations and can be calculated as follows

$$\Lambda = \frac{\epsilon}{ER_{\mathrm{part}}} \tag{6}$$

with the Young's modulus E and the microgel radius R_{part}. Appropriate values of Λ were determined by matching the adhesion radius, i.e., the radius of the contact area between the surface and the adhered particle, in experiments with the adhesion radius in simulations (cf. Figures 8 and 9A).

■ THEORY

Contact Mechanics of the Indentation in Soft Microgels on a Planar Substrate. The simplest continuum model for contact mechanics to describe the contact between two elastic bodies (here, the indenter and the microgel particle) dates back to the work of Heinrich Hertz in 1882.[32] He assumed both bodies were an infinite, homogeneous

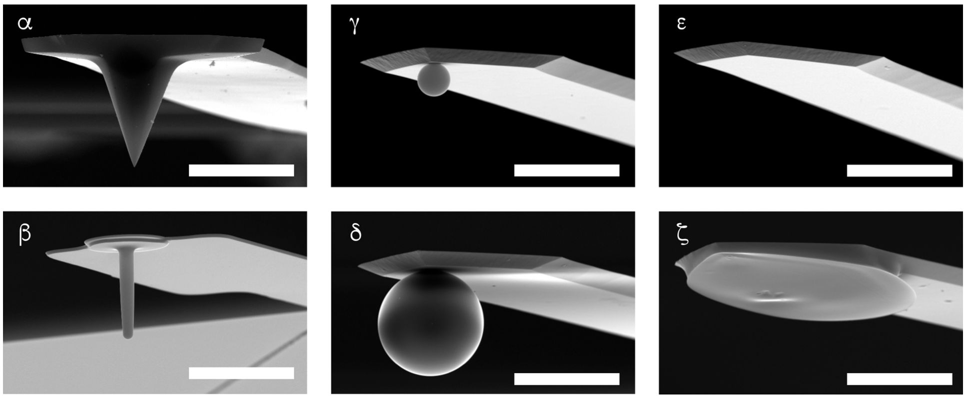

Figure 2. SEM images of six AFM cantilever-based nanoindenters: (α) sharp tip indenter (conical, $\theta = 25°$, $R < 25$ nm); (β) a rounded tip (spherical, $R = 0.99$ μm), (γ) small (spherical, $R = 3.33$ μm) and (δ) large colloidal probes (spherical, $R = 10.45$ μm); (ε) tipless (planar, tilt angle 10°) and (ζ) wedged cantilevers (planar). Scale bars represent 25 μm.

continuum and showed no interaction beyond elastic deformation like friction or adhesion. Additionally, the deformation is considered sufficiently small compared to the radii of the interacting bodies to fulfill a linear stress−strain relation. Then, the deformation δ and the force F are related by the reduced radius R_{12}, the reduced Young's modulus E_{12}, and the Poisson's ratio of the indenter and particle ν_1 and ν_2, respectively.

$$\delta = \left[\frac{3}{4}\frac{F}{E_{12}\sqrt{R_{12}}}\right]^{2/3} \Leftrightarrow F = \frac{4}{3}\sqrt{R_{12}}E_{12}\delta^{3/2} \tag{7}$$

$$\text{with: } \frac{1}{R_{12}} = \frac{1}{R_1} + \frac{1}{R_2} \text{ and } \frac{1}{E_{12}} = \frac{1-\nu_1^2}{E_1} + \frac{1-\nu_2^2}{E_2} \tag{8}$$

Considering that the indenter material is infinitely rigid compared to the sample ($E_1 \gg E_2$), the contribution of the indenter elasticity is negligible. Hence, the relation is simplified to

$$\delta = \left[\frac{3}{4}\frac{F(1-\nu_2^2)}{E_2\sqrt{R_{12}}}\right]^{2/3} \Leftrightarrow F = \frac{4}{3}\sqrt{R_{12}}\frac{E_2}{1-\nu_2^2}\delta^{3/2} \tag{9}$$

for a spherical indenter indenting a spherical microgel particle (cf. Figure 1A-I). In the case of a planar surface deforming an elastic half-sphere (cf. Figure 1A-II), the reduced radius R_{12} equals the sample radius R_2.

A similar relation between force and deformation can be stated for a rigid conical indenter (cf. Figure 1A-III).[57]

$$\delta = \left[\frac{\pi}{2}\frac{F(1-\nu_2^2)}{E_2 \tan\theta}\right]^{1/2} \Leftrightarrow F = \frac{2}{\pi}\frac{E_2}{1-\nu_2^2}\tan\theta\, \delta^2 \tag{10}$$

In this case, the cone half angle θ of the indenter defines the interaction geometry. Figure 1A sketches the indentation described by the Hertz model for the three types of indenters mentioned above.

Spherical microgel particles are typically immobilized on a planar substrate for nanoindentation. Consequently, the assumption of an elastic half-sphere becomes insufficient. When the indenter exerts a force F_{ind} onto an elastic sphere, a counterforce F_{sub} acts from the substrate to the bottom half of the microgel (cf. Figure 1B). Hence, a double contact model should be used to describe the contact elastic interaction.[11,12,38]

The simplified double contact model (SDC model) assumes that both deformations—at the indenter microgel contact δ_{12} for the sphere or δ_θ for the cone, and δ_{32} at the contact of the microgel with substrate—are independent and forces only act within the respective half-sphere. Hence, the total deformation δ is given by the sum of both half spheres (eqs 11−14). Accordingly, the deformation force relation for a sphere indenting a microgel on a planar substrate is expressed by

$$\delta = \delta_{12} + \delta_{32} = \left[\frac{3}{4}\frac{F(1-\nu_2^2)}{E_2\sqrt{R_{12}}}\right]^{2/3} + \left[\frac{3}{4}\frac{F(1-\nu_2^2)}{E_2\sqrt{R_{32}}}\right]^{2/3} \tag{11}$$

$$\delta = \delta_{12} + \delta_{32} = \left[\frac{3}{4}\frac{F(1-\nu_2^2)}{E_2\sqrt{R_{12}}}\right]^{2/3}\frac{1}{k}$$
$$\Leftrightarrow F = \frac{4}{3}\sqrt{R_{12}}\frac{E_2}{1-\nu_2^2}\delta^{3/2}k^{3/2}$$
$$\text{with } k = \frac{R_{32}^{1/3}}{R_{32}^{1/3} + R_{12}^{1/3}} \tag{12}$$

A correction factor k, which depends on the reduced radii of the microgel particle and the indenter R_{12}, and the microgel and the substrate R_{32} is introduced to account for the deviation from the single Hertzian contact in eq 9.[38] Hence, it becomes clear that the deviation of the simple Hertzian contact and the SDC model strongly depends on the dimension of the indenter and microgel particle. The deformation in both half spheres is equal for a planar indenter on a planar substrate $\delta_{12} = \delta_{32}$. Thus, the SDC model equation reduces to

$$\delta = \delta_{12} + \delta_{32} = 2\left[\frac{3}{4}\frac{F(1-\nu_2^2)}{E_2\sqrt{R_{12}}}\right]^{2/3}$$
$$\Leftrightarrow F = \frac{4}{3}\sqrt{R_{12}}\frac{E_2}{1-\nu_2^2}\left(\frac{\delta}{2}\right)^{3/2} \tag{13}$$

as $k = 0.5$.[11,58] The total deformation of a cone indenting into a microgel sphere on a planar substrate is given by the sum of the deformation caused by the cone in the upper particle half δ_θ and the bottom deformation of the particle δ_{32}.[12]

$$\delta = \delta_\theta + \delta_{32} = \left[\frac{\pi}{2}\frac{F(1-\nu_2^2)}{E_2 \tan\theta}\right]^{1/2} + \left[\frac{3}{4}\frac{F(1-\nu_2^2)}{E_2\sqrt{R_{32}}}\right]^{2/3} \tag{14}$$

In the case of cells, the spherical shape is less well fulfilled.[59] Nevertheless, the assumption of spherical shape is often used due to a lack of alternatives.[60] The SDC model has been applied to cells and cell nuclei on solid substrates.[12,40] However, the role of cell−substrate adhesion might also play an important role.

■ RESULTS

Different Indenter Geometries. Cantilevers with sharp tips and colloidal probes are currently the most commonly used indenter geometries for AFM-based nanoindentation on microgel particles. Discrepancies between data acquired with those two indenter geometries have been reported previously for microgels.[18] Similarly, deviations for the derived Young's moduli in dependence on the indenter geometry have been observed for different cell lines.[12,30,42] Here, six different indenter geometries have been utilized to study the influence on the derived Young's moduli. Moreover, due to the large statistical variation of the elastic moduli commonly observed for microgels,[18] we always measured on the same microgel particles immobilized on the substrate, however, with different nanoindenter geometries as indicated (cf. Figure 2).

Figure 2 shows SEM images of the six indenter geometries ($\alpha-\zeta$) used in this study. The selection included (α) a "classical" conical sharp tip and (β) a cantilever with a rounded tip with a radius of $R \sim 1$ μm. Conical tips (α) are characterized by their opening angle θ; however, they are not infinitely sharp but show typical tip radii of $R < 25$ nm. The rounded tip geometry (β) represents an intermediate between a conical tip and colloidal probes, which typically have radii in the order of several micrometers. Here, two different types of colloidal probes have been used: The first (γ) had radii about 3× smaller ($R \sim 3$ μm) than the latter (δ) with radii of $R \sim 10$ μm. It should be noticed that the radii of (δ) are approximately in the same order as the microgel particles to be indented. In addition, two types of tipless cantilevers have been used: (ε) a tipless cantilever that will indent under an angle of 10° and (ζ) a wedged cantilever that compensates for this angle and reduces it to about 0°.[49] In terms of the classical indenter terminology, (α) corresponds to a conical indenter, ($\beta-\delta$) to spherical indenters, and (ε,ζ) to a parallel plate. Only for PAAm, all indenter geometries have been used. In the case of POx-HASH, we did not use geometries (β) and (ζ) due to availability but not for scientific reasons.

Microgels and Nanoindentation. Two different types of microgel particles have been synthesized for this study by droplet microfluidics. The first microgel system (PAAm) was a fully synthetic covalently cross-linked polyacrylamide, which is well-established in the literature, either for particles[17,18] or for films.[61] The second microgel system (POx-HASH) has been recently introduced in the framework of inks for biofabrication and consisted of a synthetic ene-functionalized polyoxazoline (POx, a poly(ethyloxazoline-*co*-butenyloxazoline) with 10% butenyl-functionalization) and the biopolymer hyaluronic acid, which was thiol-functionalized (HASH).[46,47] Both microgel particle systems have been synthesized via droplet microfluidics, resulting in diameters in the range of 25−30 μm. The diameter of each microgel particle was determined by optical microscopy during the AFM-based nanoindentation procedure (cf. Figure 3A,B). We chose these two microgel systems fabricated by chemically different routes to verify that our findings from the nanoindentation experiments were independent of the specific microgel under investigation.

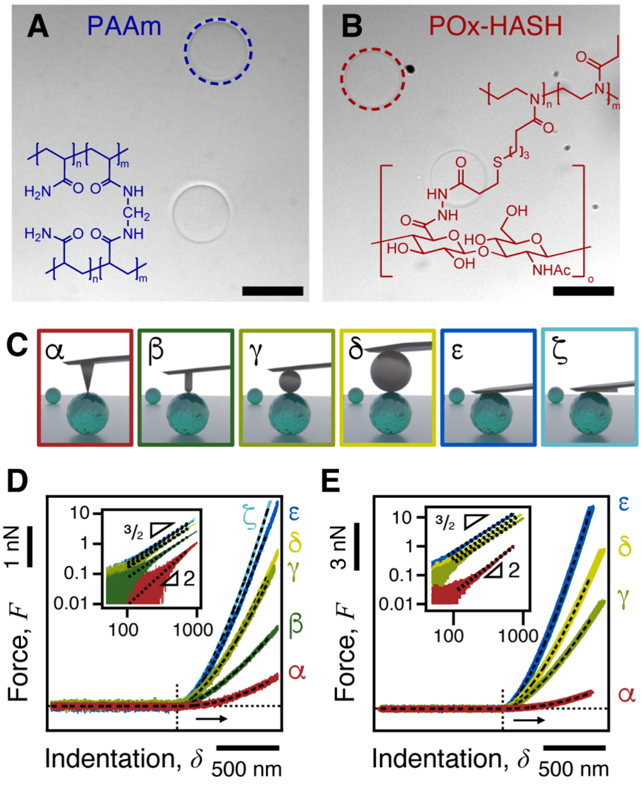

Figure 3. Brightfield optical microscopy images of (A) PAAm and (B) POx-HASH microgel particles produced via droplet microfluidics. The scale bars represent 30 μm. (C) Illustration of the experimental setup to indent the same particle with different indenter geometries $\alpha-\zeta$ by AFM: (α) sharp tip (conical) indenter; (β) a rounded tip (R = 0.99 μm), (γ) small (R = 3.33 μm) and (δ) large colloidal probes (R = 10.45 μm) (spherical); (ε) tipless and (ζ) wedged cantilevers (planar). (D,E) AFM force vs indentation curves acquired on the same (D) PAAm or (E) POx-HASH microgel particle using several nanoindenter geometries ($\alpha-\zeta/\alpha$, $\gamma-\varepsilon$). Dashed lines show fits to the Hertz model to determine the Young's modulus. The insets in (D) and (E) depict a logarithmic representation of the force vs indentation curves, which follow the expected power law coefficients of $F \sim \delta^2$ for a conical indenter (α); $F \sim \delta^{3/2}$ for spherical interaction ($\beta-\delta$) and planar compression ($\varepsilon-\zeta$).

Even though droplet microfluidic fabrication facilitates the production of microgel particles with a narrow size distribution compared to other fabrication techniques,[18] the distribution of Young's moduli can still be broad.[17,58] Therefore, we indented for a set of selected particles (n = 5), each particle with all six (PAAm) or four (POx-HASH) indenter types (cf. Figure 3C). This approach, as schematically outlined in Figure 3C, allowed us to address the influence of the indenter without having to determine the elastic moduli distribution for several hundreds of particles. It should be noticed that determining the Young's modulus of a statistically reliable number of particles with all six indenter types by nanoindentation would have been impossible timewise considering parameters like maximum indentation velocity and the requirement to center the indenter at the apex.

Table 1. Theoretical and Fitted Power Law Coefficients for the Six Indenter Types (α–ζ) According to the Hertz Model for a PAAm Microgel Particle

indenter type		sharp tip α	round tip β	small CP γ	large CP δ	tipless ε	wedged ζ
geometry		cone	sphere	sphere	sphere	planar	planar
power law coefficient	theory	2.00	1.50	1.50	1.50	1.50	1.50
	fit	2.09	1.58	1.50	1.50	1.54	1.53

In a nanoindentation experiment, the probe, i.e., the indenter, is ramped toward the microgel particle while the resulting force response is acquired simultaneously. The indentation continues until a preset trigger value is reached and the motion is reversed.[59] The resulting force vs distance profiles are then converted to force vs indentation profiles. Exemplary force vs indentation approach curves acquired at a constant ramping velocity of 0.5 μm s^{-1} and a maximal indentation depth of ~5% of the particle radius are shown in Figure 3D,E for the different indenter geometries and the two studied microgel systems: PAAm and POx-HASH, respectively. The resulting loading forces to achieve the desired deformation varied from as low as 0.5–1 nN for a conical indenter to 5–12 nN for the wedged cantilever. In general, the interaction forces increased with the size of the indenter (α to ζ) by up to an order of magnitude. It is important to notice that due to the fact that the indenter is mounted on a lever, the indentation velocity does not remain constant as the lever deflects. Hence, the ramping velocity refers to the velocity of the cantilever holder.

The dashed lines in Figure 3D,E result from fitting the force vs indention profiles to the Hertz model and the different indenter geometries. Rearranging eqs 9 and 10 shows that the force F should scale with the deformation δ by $F \sim \delta^{3/2}$ for spherical indenters, while for a conical indenter, one expects $F \sim \delta^2$. We extracted the corresponding power laws from the slopes in the logarithmic representation of the force vs indentation curves shown in the insets of Figure 3D,E. The resulting power law coefficients have been compiled in Tables 1 and 2. The good correspondence between the theoretically expected values and the values obtained from the fits corroborates the validity of the assumed indenter geometries, also for the case of the conical indenter.

Table 2. Theoretical and Fitted Power Law Coefficients for Four Indenter Types (α, γ-ε) According to the Hertz Model for a POx-HASH Microgel Particle

indenter type		sharp tip α	small CP γ	large CP δ	tipless ε
geometry		cone	sphere	sphere	planar
power law coefficient	theory	2.00	1.50	1.50	1.50
	fit	1.80	1.56	1.56	1.54

The resulting Young's moduli for sets of five PAAm and five POx-HASH microgel particles were determined according to the indentation data acquired with the different indenters (cf. Figure 4). The particle indices indicate the five particles under investigation per microgel batch. Approximately 50 force vs indentation curves acquired at the apex of the particle were evaluated for each data point, and the error bars in Figure 4 represent ± one standard deviation of the mean. Here, we compared two contact models, namely the simple Hertz model[32] that is still widely used (cf. Figure 4A-I,B-I) and the simplified double contact model (SDC model, cf. Figure 4A-II,B-II).[11,12,38] These Young's moduli based on the simple Hertz model and the SDC model have been contrasted in Figure 4. Please note that the fit quality and resulting power law dependencies are identical for indenter geometries β–ζ, and deviations are minimal for α (cf. Figure S1) for the Hertz and SDC model. Deviations in the Young's modulus arise from the different prefactors for α-ζ in eqs 12 and 14.

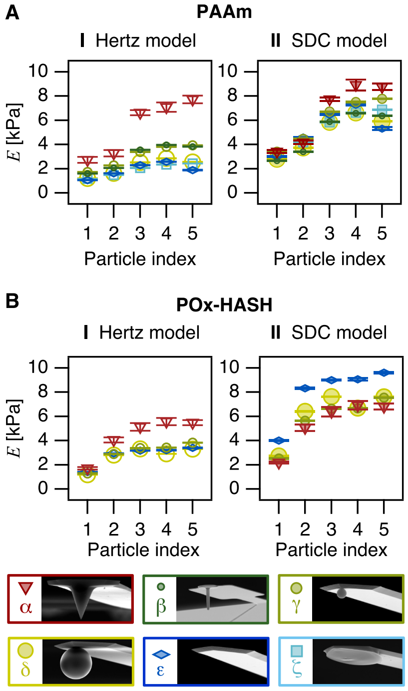

Figure 4. Young's modulus of (A) five PAAm and (B) five POx-HASH microgel particles, each characterized using a sharp tip cantilever (α), a rounded tip bio cantilever (β), a small (γ) and a large colloidal probe (δ), as well as a tipless (ε) and a wedged cantilever (ζ). I: The Young's modulus was fitted according to the Hertz model,[32] which considers only deformation at the contact of the microgel and the indenter (cf. Figure 1A, eqs 9 and 10). II: The Young's modulus was fitted using the SDC model,[11,12,38] which takes the deformation of the microgel at the contact with the indenter and the contact with the substrate into account (cf. Figure 1B, eqs 12–14). The arbitrary particle index refers to individual particles from the respective microgel batch and has been arranged according to increasing Young's moduli using the small colloidal probe (γ).

It is evident in Figure 4 that the Young's moduli determined in the framework of the Hertz model are significantly lower than for the SDC model, which was observed for both types of microgels. This difference has been expected as the indentation in the former case is completely attributed to the indentation of the probe. In contrast, in the latter case, the particle is also compressed at the contact with the planar substrate. This effect is also supposed to be more pronounced for large indenter probes, as observed here. The simple Hertz model significantly underestimates the Young's modulus of microgels at an increasing percentage up to ~64.5% compared to the SDC model when the radius of the indenter is increased to infinity.[38] Comparing the data of both models and the microgel type shows that the discrepancy in the calculated moduli for the various indenter types is significantly larger for the Hertz model. Nevertheless, some of the six indenter geometries still show different Young's moduli despite using the SDC model: The conical sharp tip indenter α and the tipless cantilever ε (POx-HASH microgel).

The conical sharp tip indenter plays a special role as it follows another power law and indents on a length scale substantially lower than the other indenters. Its cone half angle θ is the geometric parameter relevant for the elasticity determination. Due to the nanometer dimensions of the apex, the cone angle and exact tip shape are subject to large errors, even after characterization using SEM (cf. Figure S2). We measured the half angle of the sharp tip cantilever from SEM images over the relevant distance from its apex, which in our experiments is the maximum indentation depth of ~700 nm. We determined this angle to be $\theta \sim 25°$ (cf. Figure S2A). The tip shape is rounded near the apex and significantly deviates from an ideal cone. Due to these uncertainties in the determination of the tip shape, the error for Young's moduli can be up to ±10%, as shown in the Supporting Information (cf. Figure S2B). However, these errors are caused only by the inaccuracy of the cone angle determination, while the impact of the rounded tip ($R \sim 25-30$ nm) at its very end has not been accounted for. Hence, the real error caused by the tip shape is expected to be even higher. While there have been approaches to account for alterations of the tip shape at its apex in the form of blunted cone or pyramid models,[31,62,63] these approaches are not feasible for soft hydrogel networks. The associated length scales are similar to the local swollen polymeric network. Consequently, the conical indenter shape in general, along with its poor shape definition, is the most plausible cause for the large deviation of elastic moduli in Figure 4.

In the following, we will systematically exclude several other parameters that could potentially influence the observed deviation of the Young's moduli for the different indentation geometries, such as the influence of the indentation depth, the ramping velocity, and the influence of fine alignment of the indenter on the apex. However, first, we determined how much the Young's moduli varied for respective batches of microgel particles prepared by microfluidics.

Distribution of Particle Size and Young's Moduli during Synthesis. In Figure 4, the sets of microgel particles were sorted according to their Young's modulus as determined using a small colloidal probe indenter (γ). However, the elastic moduli vary significantly between the different particles for both types of microgels. Hence, we sampled about 25 particles of each type by indentation using a small colloidal probe indenter (γ). Their Young's modulus was calculated using the SDC model to estimate the elastic modulus distribution for both microgel batches. Figure 5 depicts a scatter plot of Young's moduli E, the particle radius R, and the respective distributions of either parameter. All data sets have also been evaluated using the Hertz model, and a plot contrasting the data obtained by the SDC model and Hertz model is available (cf. Figure S3). Broad distributions of elasticity in the cell-relevant sub-10 kPa regime were observed for PAAm with 6.5 ± 1.6 kPa and 7.1 ± 2.5 kPa for POx-HASH, respectively. These results underline, on the one hand, why we chose to study the impact of the indenter geometry on individual particles and thereby exclude impacts of the elasticity distribution. On the other hand, the importance of studying a statistically significant number of microgel particles is evident.

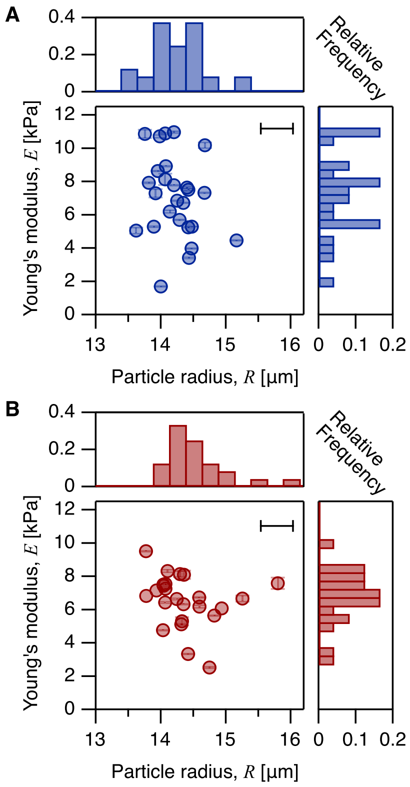

Figure 5. Scatter plot of Young's modulus E vs particle radius R for (A) PAAm and (B) POx-HASH microgels as evaluated using the SDC model. Histograms depict the distribution of the respective moduli and radii. Error bars represent the standard deviation of the mean elasticity determined from 50 curves per particle. The accuracy of the particle radius determination from optical microscopy is estimated in the upper right corner of the plots.

Influence of Indentation Velocity and Depth. It is well-known that both the indentation depth and the ramping velocity influence the derived Young's moduli of hydrogels, as demonstrated recently for ones made of PAAm.[61,64] Therefore, we varied the ramping velocity in the range of 0.1 μm s^{-1} to maximally 15 μm s^{-1} while keeping the indentation depth constant at 5% of the particle radius (cf. Figure 6A). Moreover, we varied the indentation depth between 1% and 10% of the particle radius while keeping the ramping velocity constant at 0.5 μm s^{-1} (cf. Figure 6B). Both series of experiments have been carried out using small colloidal probes (γ, $R = 3.3$ μm) as indenters. The resulting data were evaluated using the SDC model and are summarized in Figure 6 as a relative deviation concerning the standard parameters we chose for our experiments, i.e., 0.5 μm s^{-1} and 5% indentation depth, respectively. Error bars represent ± one standard deviation from 25 to 50 curves, 15 curves for the lowest ramping velocity of 0.1 μm s^{-1} on one particle. Data for additional particles and details on the evaluation are shown in the Supporting Information (cf. Figures S4 and S5).

The apparent stiffening at high tip velocities was observed for PAAm as well as for POx-HASH (cf. Figure 6C,E) and is commonly reported for hydrogels.[61,64] For both systems, the apparent stiffening is accompanied by a hysteresis between the approach and retract in the contact regime of the force curves. Representative force vs indentation curves at various ramping velocities are presented in the Supporting Information (cf. Figures S6 and S7). By contrast, at ramping velocities <1 μm s^{-1}, there is no significant difference between the approach and retraction of the cantilever, which means that the material relaxation is faster than the indenter movement, and the force response of the microgel can be considered fully elastic (cf. Figures S6A–E and S7A–E). The data shown in Figures 4 and 5 were acquired at 0.5 μm s^{-1} and thus fall clearly in the elastic regimes of both microgels.

The indentation depth represents another critical parameter in nanoindentation experiments. As an approximation, the indentation depth should not exceed 10% of the thickness of thin films.[35] For the following experiments, we varied the indentation depth in the range of ∼1%–10% of the particle radius. Exemplary force curves are presented with the respective fits to the SDC model in the Supporting Information (cf. Figures S8 and S9). For both microgels, the Young's moduli decreased with increasing indentation depth (cf. Figure 6D,F). This behavior is in stark contrast to thin films, where an increasing contribution of the substrate with increasing indentation depth is commonly reported.[33,35] One possible explanation could be an internal material gradient due to cross-linking from the outside to the inside during the microfluidic fabrication.[30] For low indentation depths (<2% of the particle radius), the data showed larger scattering, and it was not clear if the microgel interface with protruding polymer segments had been probed. Larger, spherical indenter geometries were supposed to average over surface roughness and heterogeneities. The higher consistency in curve quality and Young's modulus, obtained at a deeper indentation of 5%, provided a reasonable compromise. The effect of ramping velocity and indention depth has been studied only for one indenter type, i.e., the small colloidal probe (cf. Figure 2, colloidal probe γ). Larger probes lead to other hydrodynamic

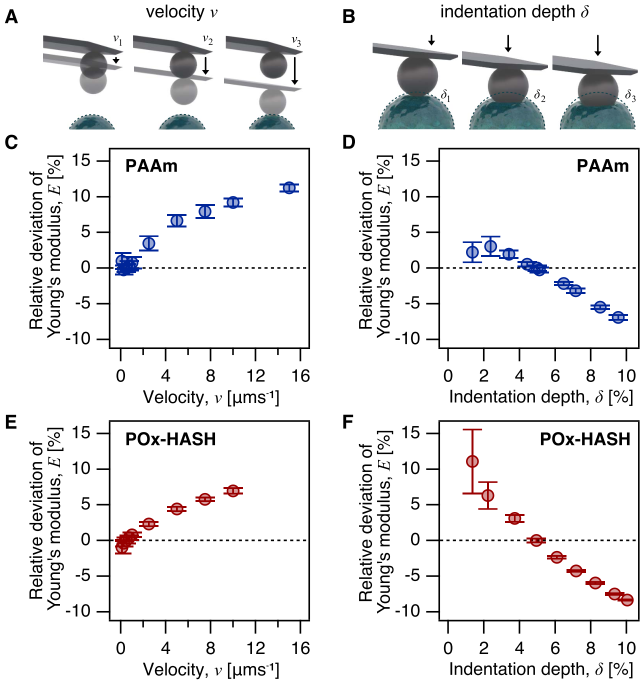

Figure 6. Influence of the ramping velocity v and the indentation depth δ on the resulting Young's modulus was studied. (A,B) Schematic illustration of the measurement parameters under investigation. The ramping velocity was varied between 0.1 μm s^{-1} and maximally 15 μm s^{-1}, and the indentation depth ranged from 1% to 10% with respect to the particle radius. Data was acquired with a small colloidal probe indenter (γ) and evaluated using the SDC model for (C,D) PAAm, and (E,F) POx-HASH microgel particles. The relative deviation of the Young's modulus is displayed with respect to the standard values used throughout this work: a ramping velocity of 0.5 μm s^{-1} and an indentation depth of 5% of the particle radius. Error bars describe ± one standard deviation of the mean from 15 to 50 curves.

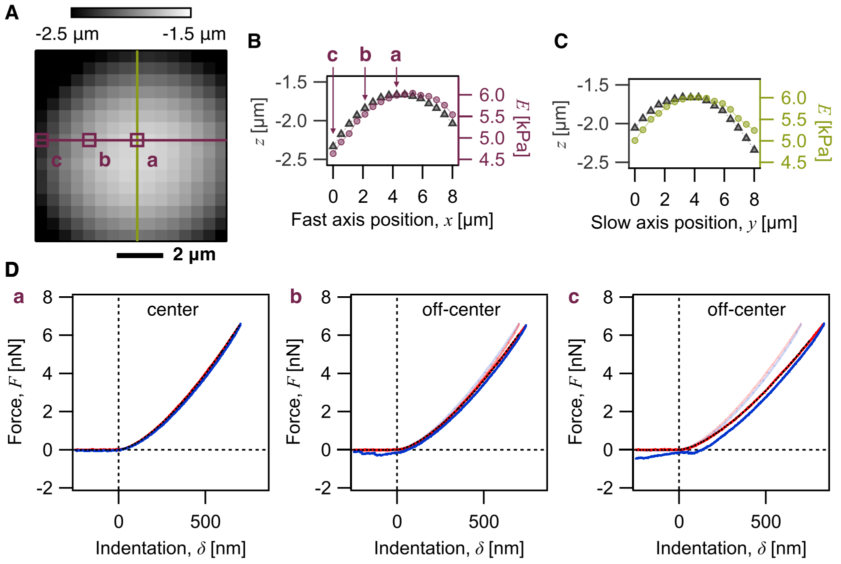

Figure 7. Alignment of the small spherical indenter (γ) to the center of the microgel bead apex. A force map consisting of 16 × 16 on an 8 μm × 8 μm area around the microgel apex has been acquired. (A) Height map shows the curvature around the microgel apex. Cross sections (green and purple lines) of the respective height data and Young's modulus (SDC model) in the direction of (B), the fast scan-axis (purple), and (C), the slow scan-axis (green) of the AFM, show that the apparent elasticity decreases with distance from the apex of the microgel. (D) Force vs indentation curves at the positions a–c as marked on the height map and the fast scan axis cross-section. The force curve acquired at the apex (a), appended to the plots of the off-center positions (b,c), highlights the deviation.

limits in terms of ramping velocity, and the interaction would result in a more punch-like interaction geometry. How far the indenter scale affects the average Young's modulus remains an open question.[43]

Position of the Indenter on the Particle. Contact mechanics, either by the Hertz or SDC model, are based on a contact of the indenter at the apex of the underlying particle. As AFM measures only the vertical force component, any misalignment will lead to errors. It should be noticed that the coarse alignment is limited by the optical resolution of the experimental setup, which is in the order of 1−2 μm. Coarse alignment was further complicated by the difference in height between the indenter and microgel before starting the force vs distance cycle. Hence, an AFM-based approach to align the center of the indenter to the apex of the microgel particle has been utilized throughout this work. We acquired an array of force curves, so-called force volume plots, around the optically identified region for the apex of the microgel. Evaluation of the height signal at the trigger point allowed the creation of a height map of the particle apex. Such a height map acquired on a PAAm microgel particle and the corresponding cross sections along the fast and slow scan axis are depicted in Figure 7A−C. The thereby achievable positional accuracy has been estimated to be $\lesssim$500 nm. We fitted a sphere cap to the height map data (cf. Figure S10A, eq S1). The extracted microgel radius of $R = 15.1$ μm agreed reasonably with the radius $R = 14.7$ μm as determined by optical microscopy (details in Supporting Information and Figure S10A). It should be highlighted that the discrepancy between the two radii falls in the realistic resolution limit of the optical microscopy in our experimental setup, including the AFM. Moreover, the sphere cap fit was based on a relatively small number of force curves in a specific area covered by the force volume plots. Hence, the radius was associated with a certain uncertainty from the fitting procedure. Additional effects, such as steric contributions, e.g. protruding polymer segments, could come into play.

Young's moduli at each position on the height map have been determined by fitting the force vs indentation curves to the SDC model (cf. Figure 7B,C). A full elasticity map depicting Young's moduli determined at each position on the grid is shown in the Supporting Information (cf. Figure S10B). A trend of apparent softening moving away from the center has been observed, which is also clearly visible in the cross sections shown in Figure 7B,C. This effect can be rationalized in terms of the slope due to the particle's topography, which leads to a decomposition of the total indentation force.[65] In addition to the apparent softer moduli away from the apex, the quality of the force vs indentation curves drastically decreases toward the outer parts of the microgel (cf. Figure 7D). Slip-off effects, visible in nonmonotonous force curves, increased.

For all experiments conducted with indenters (α−δ), the particle's apex was located by a height map, and the indenter was positioned there using the point-and-shoot function of the control software. Optical alignment was sufficient for planar indenters (ε,ζ) due to the absence of an indenter curvature. Then, force vs indentation curves for elasticity calculation were acquired at the apex of the microgel bead. This procedure was employed throughout this work to ensure precise alignment of the indenter and the microgel particle. We assume that the position accuracy was $\lesssim$500 nm due to the acquisition of force−volume plots. On this length scale, the deviation of calculated Youngs moduli is <5% and would be, therefore, most likely not be sufficient to explain the differences observed for the different indenters on the very same particle.

Substrate-Mediated Adhesion as Additional Stress during Indentation. The observed variation of the Young's modulus derived for the same particle by different indenter geometries contradicts the basic assumptions of the continuum models used to evaluate the data (cf. Figure 4). Hence, another mechanism that has not yet been accounted for must be in action. One possible mechanism would be adhesion between the microgel and the underlying substrate, leading to an additional deformation of the soft particle in the contact area with the substrate.[66] The deformation of soft hydrogel particles on substrates is well-known.[67] It should be noted that the deformation in the contact area is similar to the one encountered in the double contact model of indentation from the top. The importance of adhesion in the double contact model has already been pointed out before.[38]

To verify that adhesion is present and leads to a significant contact area, we used a technique that allowed us to visualize the contact area by optical microscopy. TIRF is an optical microscopy technique that allowed us to visualize the contact area upon fluorescence excitation in the direct vicinity of the substrate.[68] Consequently, the hydrogels had to be fluorescently labeled, which was done using the PAAm microgel system using FITC. Figure 8A displays a TIRF image of a fluorescently labeled PAAm particle immobilized on a freshly cleaned glass substrate, which has also been used for the nanoindentation measurements. In TIRF imaging, an evanescent field excites fluorophores directly on the glass/solution interface, and the bright area in Figure 8A corresponds to the contact area, being circular with a radius R_{adh} to a high degree

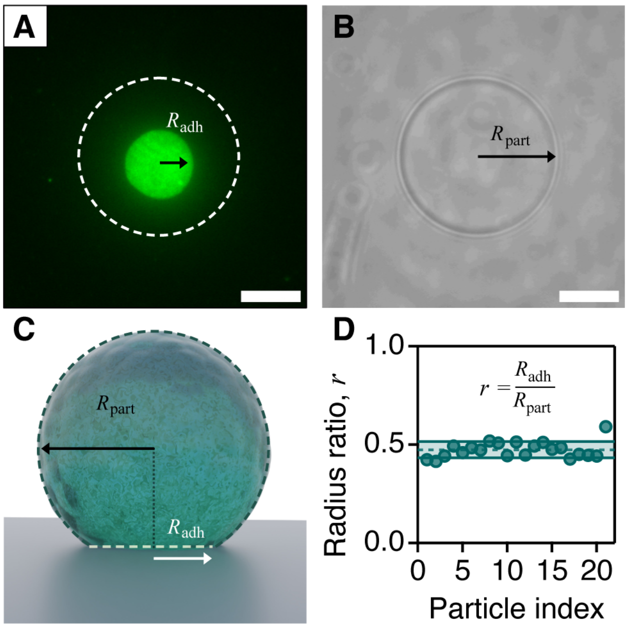

Figure 8. Determination of the contact radius of PAAm microgel particles. (A) Adhesion area and radius R_{adh}, as determined by TIRF microscopy for the particle shown in (B). Particle radius R_{part} as determined by brightfield microscopy for a fluorescence-labeled PAAm microgel particle. Scale bars represent 10 μm. (C) Schematic visualizing R_{part} and R_{adh}. (D) Distribution of the ratio R_{adh}/R_{part} for about 20 particles. The lines represent the average (dashed) and ± one standard deviation of the mean (solid), respectively.

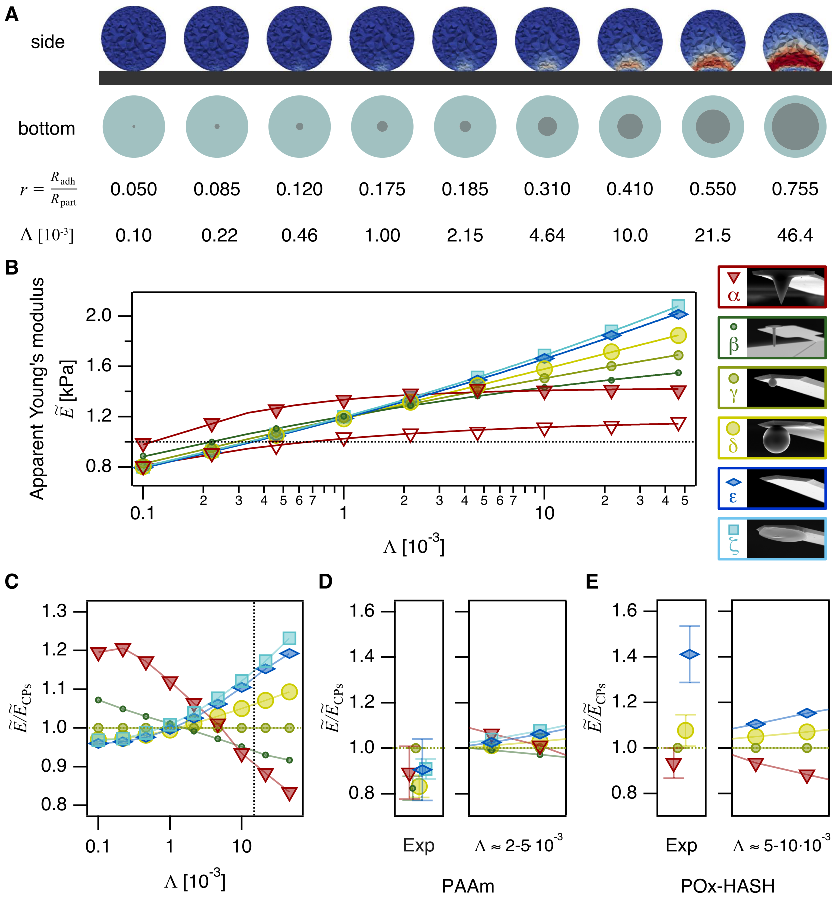

Figure 9. (A) Simulation of the prestress on the microgels due to the adhesive contact with the substrate (side view). The color scale indicates the stress within the microgel particle due to adhesion. The dimensionless parameter Λ is used to describe the adhesive strength. The resulting adhesive contact area (gray) with respect to the microgel size (blue) is illustrated in a bottom-view perspective. The ratio $r = R_{\mathrm{adh}}/R_{\mathrm{part}}$ characterizes the area of the adhesive contact. (B) The apparent Young's moduli $\tilde{E}$ as received from the simulation for a particle with a Young's modulus of 1 kPa for indenters α-ζ depends on Λ. Closed symbols represent the SDC model, open triangles refer to the Hertz data for the conical indenter. (C) Normalization of the apparent Young's modulus from simulation to the small colloidal probe (γ). (D,E) Normalized experimental Young's moduli and approximate range of Λ to describe the data from the simulation for (D) PAAm and (E) POx-HASH microgels. Mean values ± one standard deviation of the mean from five particles (cf. Figure 4) for each indenter geometry are presented.

of approximation. Figure 8B shows the corresponding brightfield image, which has been used to determine the actual particle radius R_{part}. Figure 8C illustrates the adhesive contact between a microgel particle and the glass substrate with the contact radius R_{adh} and the particle radius R_{part}. We used the ratio $r = R_{\mathrm{adh}}/R_{\mathrm{part}}$ to characterize the adhesive properties of the FITC-labeled PAAm microgels on the glass surface. Evaluating about 20 particles resulted in a value of $r = 0.47 \pm 0.04$. These data are summarized in Figure 8D. It should be noted that the fluorescently labeled PAAm is more positively charged than the pristine PAAm, as determined by lipid adsorption experiments (data not shown). Hence, we see the value of $r = 0.47$ as the upper limit for the predeformation of the PAAm microgels characterized by nanoindentation due to adhesion.

Modeling Adhesion. We performed theoretical simulations to evaluate the effect of adhesion on the predeformation of microgel particles. In order to map the adhesive properties in the simulation, we used a simple model based on the dimensionless number Λ defined in eq 6 above

$$\Lambda = \frac{\epsilon}{ER_{\mathrm{part}}} \tag{15}$$

Λ is a dimensionless number modeling the ratio between adhesion forces and elastic particle forces. Here, ϵ is the Lennard-Jones potential constant, as defined in eq 5 above, which is responsible for adhesion to the substrate. According to our simulations based on the finite element method, the microgel particle deforms even without an external force, as depicted in Figure 9A. The adhesive contact area of radius R_{adh} increased as expected with Λ (cf. Figure S11). We fitted a power law to determine Λ corresponding to the experimental value $r = 0.47$ as determined by the TIRF data (details in the Supporting Information S6, Figure S11), which resulted in $\Lambda \approx 0.015$. However, it should be highlighted that nonlabeled PAAm microgels showed weaker adhesion, leading to smaller Λ values.

Indenter Geometry and Adhesion. After equilibrating the microgels on the adhesive substrates, the deformation using the respective six different indenter geometries (α–ζ) was simulated. An opening angle of 25° for the conical indenter (α), radii of 0.99 μm the rounded tip (β), and 3.3 μm, 10.5 μm for the colloidal probes (γ,δ); and a tilt angle of 10° for the tipless and 0° for the wedged cantilever have been utilized in agreement with the experimental conditions. The force vs deformation data from the numerical simulations have been fitted to the SDC model similarly to the experimental data. The resulting apparent Young's moduli $\tilde{E}$ from the fits to eqs 12 and 14, respectively, are summarized in Figure 9B as a function of Λ. In the case of the conical indenter, the classical Hertz model (open triangles) is shown in addition to the SDC model (closed triangles). The simulated force vs indentation curves and fits are available in Figures S12 and S13 in the Supporting Information. It is evident that depending on the geometry and type of the indenter, the apparent elastic modulus deviated from the Young's modulus, which was set to 1 kPa for the simulation. With stronger adhesion, i.e., higher values of Λ, the deviation between the different indenter geometries became more pronounced, especially for larger geometries, like the large colloidal probe (δ) and the planar indenters (ε,ζ).

The nonlinear dependence between the apparent elastic moduli and the adhesion for the different indenter geometries provides an explanation for the observed deviations in the experimental data for both types of microgels (cf. Figure 4). It should be pointed out that the Young's moduli reported in Figure 9B are only apparent elastic properties originating from fitting simulated data for particles with a homogeneous "true" Young's modulus of 1 kPa. However, in the simulation, the elastic properties scale linearly and are, therefore, also valid for the higher elastic modulus of the experimentally studied particles and allow further semiquantitative analysis: We normalized the apparent Young's moduli from the simulation $\tilde{E}$ to the small colloidal probe data $\tilde{E}_{\mathrm{CPs}}$, i.e., the simulations for geometry γ (cf. Figure 9C). Figure 9D,E show the same normalization for the experimental data, i.e., $\tilde{E}/\tilde{E}_{\mathrm{CPs}}$. The data reported in Figure 9D, E were averaged over all five particles of each type of microgel from Figure 4. The separate data for all individual particles are available in the Supporting Information (cf. Figure S14). The normalized apparent Young's moduli $\tilde{E}/\tilde{E}_{\mathrm{CPs}}$ in Figure 9D for PAAm microgels are clustered, approximately corresponding to the simulation data for $\Lambda = 2{-}5 \times 10^{-3}$. By contrast, the data for POx-HASH in Figure 9E are more compatible with $\Lambda = 5{-}10 \times 10^{-3}$. While an accurate quantitative match between simulation and experimental values is not to be expected due to the qualitative nature of our adhesion model and the parameter Λ, there is a good qualitative match for the normalized Young's moduli with respect to the different indenter geometries if one considers the effect of adhesion and utilizes the SDC model.

■ CONCLUSIONS

The SDC model represents a more realistic description of the elastic properties of microgel particles than the classical Hertz model, which is still widely used to quantitatively report Young's moduli as determined by AFM-based nanoindentation. Our study on two different microgel model systems also demonstrates that adhesion plays an important role in the quantitative description by SDC model. Moreover, the prestress between particle and substrate due to adhesion provides an explanation for the variation in the elastic moduli as determined by different indenter geometries by means of the SDC model. The microgel particles studied here, prepared by microfluidics, are similar to cells in many aspects, albeit better defined in their physical properties. Nevertheless, our results should also be helpful for the characterization of cells. However, for cells, the incorporation of adhesion in the double contact model will be even more important. We are not aware of such models, and the numerical simulations presented here are not a fully adequate replacement. In the future, the SDC model might also become important to analyze experiments that probe the dynamic nanoindentation of hydrogels,[69,70] especially for microgel particles.

The long-standing question of the best-suited indenter geometry, which has been discussed extensively in the literature, can be reduced in the framework of the SDC model to more practical aspects. We suggest the following approach: (i) Adhesion effects are less pronounced for small indenter dimensions, such as sharp conical tips, rounded tips, or small colloidal probes. However, the exact geometrical dimension will be less-well traceable for conical indenters, and the indentation depth will be limited for rounded tips. In this respect, small colloidal probes, which allow a sufficient indentation depth without violating the small indentation limitation of the Hertzian contact mechanics, should be the best compromise for practical purposes.

Based on the experimental findings, (ii) we encourage the use of force volume measurements to enhance the alignment precision compared to the optical alignment of the indenter and sample. Thereby, the underestimation of the Young's modulus by off-center data acquisition should be minimized. Moreover, (iii) measurement parameters like the indentation depth and velocity can impact the accuracy and comparability of the reported moduli. The herein-presented values can be helpful as starting points; however, they cannot entirely replace reassessment for the chosen combination of sample and indenter. Finally, (iv) accurately reporting all experimental parameters like indenter and sample radii, indentation depth, and velocity, calibration of instrument sensitivity, and spring constants improves the cross-study comparability of AFM-based elasticity measurements.

■ ASSOCIATED CONTENT

Supporting Information

The Supporting Information is available free of charge at https://pubs.acs.org/doi/10.1021/acsanm.4c06964.

> Additional experimental methods; impact of the half angle on the Young's modulus determination using the conical indenter; distribution of Young's moduli evaluated with SDC model and Hertz model; details on the influence of ramping velocity and indentation depth on the Young's moduli; sphere cap fit to the height map and Young's modulus distribution at the apex of the microgel particle; simulations of the adhesive contact and resulting deformations (PDF)

■ AUTHOR INFORMATION

Corresponding Author

Georg Papastavrou − *Department of Physical Chemistry II − Interfaces and Nanoanalytics, University of Bayreuth, 95447 Bayreuth, Germany; Bavarian Polymer Institute and Bayreuth Center for Colloids and Interfaces, Bayreuth Center for Molecular Biosciences, Bayreuth Center for Material Science and Engineering, University of Bayreuth, 95447 Bayreuth, Germany;* orcid.org/0000-0002-5870-6693; Email: georg.papastavrou@uni-bayreuth.de

Authors

Nadine Raßmann – *Department of Physical Chemistry II – Interfaces and Nanoanalytics, University of Bayreuth, 95447 Bayreuth, Germany;* orcid.org/0000-0002-8924-4444

Steffen Trippmacher – *Department of Physical Chemistry II – Interfaces and Nanoanalytics, University of Bayreuth, 95447 Bayreuth, Germany*

Agnes Specht – *Department of Physical Chemistry II – Interfaces and Nanoanalytics, University of Bayreuth, 95447 Bayreuth, Germany*

Katinka Theis – *Department for Functional Medicine and Dentistry, University of Hospital of Würzburg, 97070 Würzburg, Germany*

Tamino Rößler – *Department of Physical Chemistry II – Interfaces and Nanoanalytics, University of Bayreuth, 95447 Bayreuth, Germany*

Sebastian Wohlrab – *Biofluid Simulation and Modeling, Theoretische Physik VI, University of Bayreuth, 95447 Bayreuth, Germany*

Richard Kellnberger – *Biofluid Simulation and Modeling, Theoretische Physik VI, University of Bayreuth, 95447 Bayreuth, Germany;* orcid.org/0009-0003-1782-4735

Sahar Salehi – *Department of Biomaterials, University of Bayreuth, 95447 Bayreuth, Germany;* orcid.org/0000-0002-6740-4195

Hendrik Bargel – *Department of Biomaterials, University of Bayreuth, 95447 Bayreuth, Germany*

Nicolas Helfricht – *Department of Physical Chemistry II – Interfaces and Nanoanalytics, University of Bayreuth, 95447 Bayreuth, Germany; Bavarian Polymer Institute, University of Bayreuth, 95447 Bayreuth, Germany;* orcid.org/0000-0002-5839-9670

Krystyna Albrecht – *Department for Functional Medicine and Dentistry, University of Hospital of Würzburg, 97070 Würzburg, Germany*

Thomas Scheibel – *Department of Biomaterials, University of Bayreuth, 95447 Bayreuth, Germany; Bavarian Polymer Institute and Bayreuth Center for Colloids and Interfaces, Bayreuth Center for Molecular Biosciences, Bayreuth Center for Material Science and Engineering, University of Bayreuth, 95447 Bayreuth, Germany; Faculty of Medicine, University of Würzburg, 97070 Würzburg, Germany*

Jürgen Groll – *Department for Functional Medicine and Dentistry, University of Hospital of Würzburg, 97070 Würzburg, Germany; Faculty of Medicine and Bavarian Polymer Institute, University of Würzburg, 97070 Würzburg, Germany;* orcid.org/0000-0003-3167-8466

Stephan Gekle – *Biofluid Simulation and Modeling, Theoretische Physik VI, University of Bayreuth, 95447 Bayreuth, Germany;* orcid.org/0000-0001-5597-1160

Complete contact information is available at: https://pubs.acs.org/10.1021/acsanm.4c06964

Author Contributions

○Nadine Raßmann and Steffen Trippmacher contributed equally.

Notes

The authors declare no competing financial interest.

■ ACKNOWLEDGMENTS

The authors thank Sebastian Sittl for help with the SEM images of the cantilevers and the Keylab Electron Microscopy of Bavarian Polymer Institute (BPI). Funding by the Deutsche Forschungsgemeinschaft (DFG, German Research Foundation) - Projekt Nummer 326998133-TRR225 (subprojects A08, B03 and B07) is gratefully acknowledged. Calculations were performed using the festus-cluster of the Bayreuth Centre for High Performance Computing funded by the Deutsche Forschungsgemeinschaft (DFG, German Research Foundation) - 523317330. N.R., S.T., A.S., and T.R. thank the Elite Network Bavaria (ENB) for support within the program "Macromolecular Science".

■ REFERENCES

(1) Hao, Y.; Cheng, S.; Tanaka, Y.; Hosokawa, Y.; Yalikun, Y.; Li, M. Mechanical properties of single cells: Measurement methods and applications. *Biotechnol. Adv.* **2020**, *45*, 107648.

(2) Urbanska, M.; Muñoz, H. E.; Shaw Bagnall, J.; Otto, O.; Manalis, S. R.; Di Carlo, D.; Guck, J. A comparison of microfluidic methods for high-throughput cell deformability measurements. *Nat. Methods* **2020**, *17* (6), 587–593.

(3) Yi, B.; Xu, Q.; Liu, W. An overview of substrate stiffness guided cellular response and its applications in tissue regeneration. *Bioactive Mater.* **2022**, *15*, 82–102.

(4) Vining, K. H.; Mooney, D. J. Mechanical forces direct stem cell behaviour in development and regeneration. *Nat. Rev. Mol. Cell Biol.* **2017**, *18* (12), 728–742.

(5) Lekka, M.; Laidler, P.; Gil, D.; Lekki, J.; Stachura, Z.; Hrynkiewicz, A. Z. Elasticity of normal and cancerous human bladder cells studied by scanning force microscopy. *Eur. Biophys. J.* **1999**, *28* (4), 312–316.

(6) Radman, B. A.; Alhameed, A. M. M.; Shu, G.; Yin, G.; Wang, M. Cellular elasticity in cancer: a review of altered biomechanical features. *J. Mater. Chem. B* **2024**, *12* (22), 5299–5324.

(7) Zemla, J.; Danilkiewicz, J.; Orzechowska, B.; Pabijan, J.; Seweryn, S.; Lekka, M. Atomic force microscopy as a tool for assessing the cellular elasticity and adhesiveness to identify cancer cells and tissues. *Semin. Cell Dev. Biol.* **2018**, *73*, 115–124.

(8) Costa, K. D. Single-cell elastography: probing for disease with the atomic force microscope. *Dis. Markers* **2004**, *19* (2–3), 139–154.

(9) Pérez-Domínguez, S.; Kulkarni, S. G.; Pabijan, J.; Gnanachandran, K.; Holuigue, H.; Eroles, M.; Lorenc, E.; Berardi, M.; Antonovaite, N.; Marini, M. L.; Lopez Alonso, J.; Redondo-Morata, L.; Dupres, V.; Janel, S.; Acharya, S.; Otero, J.; Navajas, D.; Bielawski, K.; Schillers, H.; Lafont, F.; Rico, F.; Podestà, A.; Radmacher, M.; Lekka, M. Reliable, standardized measurements for cell mechanical properties. *Nanoscale* **2023**, *15* (40), 16371–16380.

(10) Fortier, H.; Variola, F.; Wang, C.; Zou, S. AFM force indentation analysis on leukemia cells. *Anal. Methods* **2016**, *8* (22), 4421–4431.

(11) Dokukin, M. E.; Guz, N. V.; Sokolov, I. Quantitative study of the elastic modulus of loosely attached cells in AFM indentation experiments. *Biophys. J.* **2013**, *104* (10), 2123–2131.

(12) Daza, R.; González-Bermúdez, B.; Cruces, J.; De la Fuente, M.; Plaza, G. R.; Arroyo-Hernández, M.; Elices, M.; Pérez-Rigueiro, J.; Guinea, G. V. Comparison of cell mechanical measurements provided by Atomic Force Microscopy (AFM) and Micropipette Aspiration (MPA). *J. Mech. Behav. Biomed. Mater.* **2019**, *95*, 103–115.

(13) Ding, Y.; Xu, G. K.; Wang, G. F. On the determination of elastic moduli of cells by AFM based indentation. *Sci. Rep.* **2017**, *7*, 45575.

(14) Raz, N.; Li, J. K.; Fiddes, L. K.; Tumarkin, E.; Walker, G. C.; Kumacheva, E. Microgels with an Interpenetrating Network Structure as a Model System for Cell Studies. *Macromolecules* **2010**, *43* (17), 7277–7281.

(15) Kumachev, A.; Tumarkin, E.; Walker, G. C.; Kumacheva, E. Characterization of the mechanical properties of microgels acting as cellular microenvironments. *Soft Matter* **2013**, *9* (10), 2959.

(16) Kim, E.; Lee, H. Mechanical characterization of soft microparticles prepared by droplet microfluidics. *J. Polym. Sci.* **2022**, *60* (11), 1670−1699.

(17) Labriola, N. R.; Mathiowitz, E.; Darling, E. M. Fabricating polyacrylamide microbeads by inverse emulsification to mimic the size and elasticity of living cells. *Biomater. Sci.* **2017**, *5* (1), 41−45.

(18) Girardo, S.; Träber, N.; Wagner, K.; Cojoc, G.; Herold, C.; Goswami, R.; Schlüßler, R.; Abuhattum, S.; Taubenberger, A.; Reichel, F.; Mokbel, D.; Herbig, M.; Schürmann, M.; Müller, P.; Heida, T.; Jacobi, A.; Ulbricht, E.; Thiele, J.; Werner, C.; Guck, J. Standardized microgel beads as elastic cell mechanical probes. *J. Mater. Chem. B* **2018**, *6* (39), 6245−6261.

(19) Li, W.; Zhang, L.; Ge, X.; Xu, B.; Zhang, W.; Qu, L.; Choi, C. H.; Xu, J.; Zhang, A.; Lee, H.; Weitz, D. A. Microfluidic fabrication of microparticles for biomedical applications. *Chem. Soc. Rev.* **2018**, *47* (15), 5646−5683.

(20) Heida, T.; Neubauer, J. W.; Seuss, M.; Hauck, N.; Thiele, J.; Fery, A. Mechanically Defined Microgels by Droplet Microfluidics. *Macromol. Chem. Phys.* **2017**, *218* (2), 1600418.

(21) Oyen, M. L. Mechanical characterisation of hydrogel materials. *Int. Mater. Rev.* **2014**, *59* (1), 44−59.

(22) Backes, S.; Von Klitzing, R. Nanomechanics and Nanorheology of Microgels at Interfaces. *Polymers* **2018**, *10* (9), 978.

(23) Kilpatrick, J. I.; Revenko, I.; Rodriguez, B. J. Nanomechanics of Cells and Biomaterials Studied by Atomic Force Microscopy. *Adv. Healthcare Mater.* **2015**, *4* (16), 2456−2474.

(24) Mietke, A.; Otto, O.; Girardo, S.; Rosendahl, P.; Taubenberger, A.; Golfier, S.; Ulbricht, E.; Aland, S.; Guck, J.; Fischer-Friedrich, E. Extracting Cell Stiffness from Real-Time Deformability Cytometry: Theory and Experiment. *Biophys. J.* **2015**, *109* (10), 2023−2036.

(25) Müller, S. J.; Weigl, F.; Bezold, C.; Bächer, C.; Albrecht, K.; Gekle, S. A hyperelastic model for simulating cells in flow. *Biomech. Model. Mechanobiol.* **2021**, *20* (2), 509−520.

(26) Huber, D.; Oskooei, A.; Casadevall I Solvas, X.; deMello, A.; Kaigala, G. V. Hydrodynamics in Cell Studies. *Chem. Rev.* **2018**, *118* (4), 2042−2079.

(27) González-Bermúdez, B.; Guinea, G. V.; Plaza, G. R. Advances in Micropipette Aspiration: Applications in Cell Biomechanics, Models, and Extended Studies. *Biophys. J.* **2019**, *116* (4), 587−594.

(28) Harris, A. R.; Charras, G. T. Experimental validation of atomic force microscopy-based cell elasticity measurements. *Nanotechnology* **2011**, *22* (34), 345102.

(29) Thomas-Chemin, O.; Séverac, C.; Trévisiol, E.; Dague, E. Indentation of living cells by AFM tips may not be what we thought. *Micron* **2023**, *174*, 103523.

(30) Zemla, J.; Bobrowska, J.; Kubiak, A.; Zieliński, T.; Pabijan, J.; Pogoda, K.; Bobrowski, P.; Lekka, M. Indenting soft samples (hydrogels and cells) with cantilevers possessing various shapes of probing tip. *Eur. Biophys. J.* **2020**, *49* (6), 485−495.

(31) Rico, F.; Roca-Cusachs, P.; Gavara, N.; Farré, R.; Rotger, M.; Navajas, D. Probing mechanical properties of living cells by atomic force microscopy with blunted pyramidal cantilever tips. *Phys. Rev. E* **2005**, *72* (2), 021914.

(32) Hertz, H. Ueber die Berührung fester elastischer Körper. *J. Reine Angew. Math.* **1882**, *1882* (92), 156−171.

(33) Miyake, K.; Satomi, N.; Sasaki, S. Elastic modulus of polystyrene film from near surface to bulk measured by nanoindentation using atomic force microscopy. *Appl. Phys. Lett.* **2006**, *89* (3), 031925.

(34) Akhremitchev, B. B.; Walker, G. C. Finite Sample Thickness Effects on Elasticity Determination Using Atomic Force Microscopy. *Langmuir* **1999**, *15* (17), 5630−5634.

(35) Domke, J.; Radmacher, M. Measuring the Elastic Properties of Thin Polymer Films with the Atomic Force Microscope. *Langmuir* **1998**, *14* (12), 3320−3325.

(36) Dimitriadis, E. K.; Horkay, F.; Maresca, J.; Kachar, B.; Chadwick, R. S. Determination of elastic moduli of thin layers of soft material using the atomic force microscope. *Biophys. J.* **2002**, *82* (5), 2798−2810.

(37) Burmistrova, A.; Richter, M.; Eisele, M.; Üzüm, C.; von Klitzing, R. The Effect of Co-Monomer Content on the Swelling/Shrinking and Mechanical Behaviour of Individually Adsorbed PNIPAM Microgel Particles. *Polymers* **2011**, *3* (4), 1575−1590.

(38) Glaubitz, M.; Medvedev, N.; Pussak, D.; Hartmann, L.; Schmidt, S.; Helm, C. A.; Delcea, M. A novel contact model for AFM indentation experiments on soft spherical cell-like particles. *Soft Matter* **2014**, *10* (35), 6732−6741.

(39) Berry, J. D.; Biviano, M.; Dagastine, R. R. Poroelastic properties of hydrogel microparticles. *Soft Matter* **2020**, *16* (22), 5314−5324.

(40) Chang, D.; Hirate, T.; Uehara, C.; Maruyama, H.; Uozumi, N.; Arai, F. Evaluating Young's Modulus of Single Yeast Cells Based on Compression Using an Atomic Force Microscope with a Flat Tip. *Microsc. Microanal.* **2021**, *27* (2), 392−399.

(41) Rosenhek-Goldian, I.; Cohen, S. R. Some considerations in nanoindentation measurement and analysis by atomic force microscopy. *J. Vac. Sci. Technol. A* **2023**, *41* (6), 062801.

(42) Chiou, Y. W.; Lin, H. K.; Tang, M. J.; Lin, H. H.; Yeh, M. L. The influence of physical and physiological cues on atomic force microscopy-based cell stiffness assessment. *PLoS One* **2013**, *8* (10), e77384.

(43) Kulkarni, S. G.; Pérez-Domínguez, S.; Radmacher, M. Influence of cantilever tip geometry and contact model on AFM elasticity measurement of cells. *J. Mol. Recognit.* **2023**, *36* (7), e3018.

(44) Managuli, V.; Roy, S. Influencing Factors in Atomic Force Microscopy Based Mechanical Characterization of Biological Cells. *Exp. Tech.* **2017**, *41* (6), 673−687.

(45) Stylianou, A.; Mpekris, F.; Voutouri, C.; Papoui, A.; Constantinidou, A.; Kitiris, E.; Kailides, M.; Stylianopoulos, T. Nanomechanical properties of solid tumors as treatment monitoring biomarkers. *Acta Biomater.* **2022**, *154*, 324−334.

(46) Reineke, B.; Paulus, I.; Löffelsend, S.; Yu, C. H.; Vinogradov, D.; Meyer, A.; Hazur, J.; Röder, J.; Vollmer, M.; Tamgüney, G.; Hauschild, S.; Boccaccini, A. R.; Groll, J.; Förster, S. On-chip fabrication and in-flow 3D-printing of microgel constructs: from chip to scaffold materials in one integral process. *Biofabrication* **2024**, *16* (2), 025038.

(47) Brand, J. S.; Forster, L.; Böck, T.; Stahlhut, P.; Teßmar, J.; Groll, J.; Albrecht, K. Covalently Cross-Linked Pig Gastric Mucin Hydrogels Prepared by Radical-Based Chain-Growth and Thiol-ene Mechanisms. *Macromol. Biosci.* **2022**, *22* (4), e2100274.

(48) Hu, X.; Tong, Z.; Lyon, L. A. Synthesis and Physicochemical Properties of Cationic Microgels Based on Poly(N-isopropylmethacrylamide). *Colloid Polym. Sci.* **2011**, *289* (3), 333−339.

(49) Stewart, M. P.; Hodel, A. W.; Spielhofer, A.; Cattin, C. J.; Müller, D. J.; Helenius, J. Wedged AFM-cantilevers for parallel plate cell mechanics. *Methods* **2013**, *60* (2), 186−194.

(50) Hutter, J. L.; Bechhoefer, J. Calibration of atomic-force microscope tips. *Rev. Sci. Instrum.* **1993**, *64* (7), 1868−1873.

(51) Heim, L.-O.; Rodrigues, T. S.; Bonaccurso, E. Direct thermal noise calibration of colloidal probe cantilevers. *Colloids Surf., A* **2014**, *443*, 377−383.

(52) Boudou, T.; Ohayon, J.; Picart, C.; Tracqui, P. An extended relationship for the characterization of Young's modulus and Poisson's ratio of tunable polyacrylamide gels. *Biorheology* **2007**, *44* (2), 139.

(53) Takigawa, T.; Morino, Y.; Urayama, K.; Masuda, T. Poisson's ratio of polyacrylamide (PAAm) gels. *Polym. Gels Netw.* **1996**, *4* (1), 1−5.

(54) Geuzaine, C.; Remacle, J. Gmsh: A 3-D finite element mesh generator with built-in pre- and post-processing facilities. *Int. J. Numer. Methods Eng.* **2009**, *79* (11), 1309−1331.

(55) Bower, A. F. *Applied Mechanics of Solids*, 1 ed.; CRC Press, 2009.

(56) Frenkel, D.; Smit, B. *Understanding Molecular Simulation*, 2 ed.; Elsevier, 2002.

(57) Sneddon, I. N. The relation between load and penetration in the axisymmetric boussinesq problem for a punch of arbitrary profile. *Int. J. Eng. Sci.* **1965**, *3* (1), 47−57.

https://doi.org/10.1021/acsanm.4c06964
ACS Appl. Nano Mater. XXXX, XXX, XXX−XXX

(58) Hidaka, K.; Moine, L.; Collin, G.; Labarre, D.; Louis Grossiord, J.; Huang, N.; Osuga, K.; Wada, S.; Laurent, A. Elasticity and viscoelasticity of embolization microspheres. *J. Mech. Behav. Biomed. Mater.* **2011**, *4* (8), 2161−2167.

(59) Krieg, M.; Fläschner, G.; Alsteens, D.; Gaub, B. M.; Roos, W. H.; Wuite, G. J. L.; Gaub, H. E.; Gerber, C.; Dufrêne, Y. F.; Müller, D. J. Atomic force microscopy-based mechanobiology. *Nat. Rev. Phys.* **2019**, *1*, 41−57.

(60) Lomakina, E. B.; Spillmann, C. M.; King, M. R.; Waugh, R. E. Rheological analysis and measurement of neutrophil indentation. *Biophys. J.* **2004**, *87* (6), 4246−4258.

(61) Simic, R.; Mathis, C. H.; Spencer, N. D. A two-step method for rate-dependent nano-indentation of hydrogels. *Polymer* **2018**, *137*, 276−282.

(62) Owen, D. S. Toward a better modulus at shallow indentations-Enhanced tip and sample characterization for quantitative atomic force microscopy. *Microsc. Res. Tech.* **2023**, *86* (1), 84−96.

(63) Boccaccio, A.; Papi, M.; De Spirito, M.; Lamberti, L.; Pappalettere, C. Effect of the residual stress on soft sample nanoindentation. *Appl. Phys. Lett.* **2013**, *102* (13), 133704.

(64) Huth, S.; Sindt, S.; Selhuber-Unkel, C. Automated analysis of soft hydrogel microindentation: Impact of various indentation parameters on the measurement of Young's modulus. *PLoS One* **2019**, *14* (8), e0220281.

(65) Grafström, S.; Ackermann, J.; Hagen, T.; Neumann, R.; Probst, O. Analysis of lateral force effects on the topography in scanning force microscopy. *J. Vac. Sci. Technol. B* **1994**, *12* (3), 1559−1564.

(66) Johnson, K. L.; Kendall, K.; D, R. A. Surface energy and the contact of elastic solids. *Proc. R. Soc. Lond. A* **1971**, *324* (1558), 301−313.

(67) Wang, H.; Jacobi, F.; Waschke, J.; Hartmann, L.; Löwen, H.; Schmidt, S. Elastic Modulus Dependence on the Specific Adhesion of Hydrogels. *Adv. Funct. Mater.* **2017**, *27* (41), 1702040.

(68) Fish, K. N. Total Internal Reflection Fluorescence (TIRF) Microscopy. *Curr. Proc.* **2022**, *2* (8), e517.

(69) Nalam, P. C.; Gosvami, N. N.; Caporizzo, M. A.; Composto, R. J.; Carpick, R. W. Nano-rheology of hydrogels using direct drive force modulation atomic force microscopy. *Soft Matter* **2015**, *11* (41), 8165−8178.

(70) Wang, H.; Liu, Y.-Q.; Hang, J.-T.; Xu, G.-K.; Feng, X.-Q. Dynamic high-order buckling and spontaneous recovery of active epithelial tissues. *J. Mech. Phys. Solids* **2024**, *183*, 105496.

https://doi.org/10.1021/acsanm.4c06964